The effect of collisions on the multi-fluid plasma Richtmyer–Meshkov instability

K. C. Tapinou, V. Wheatley, D. Bond, et al.

View Online

Export Citation

CrossMark

ARTICLES YOU MAY BE INTERESTED IN

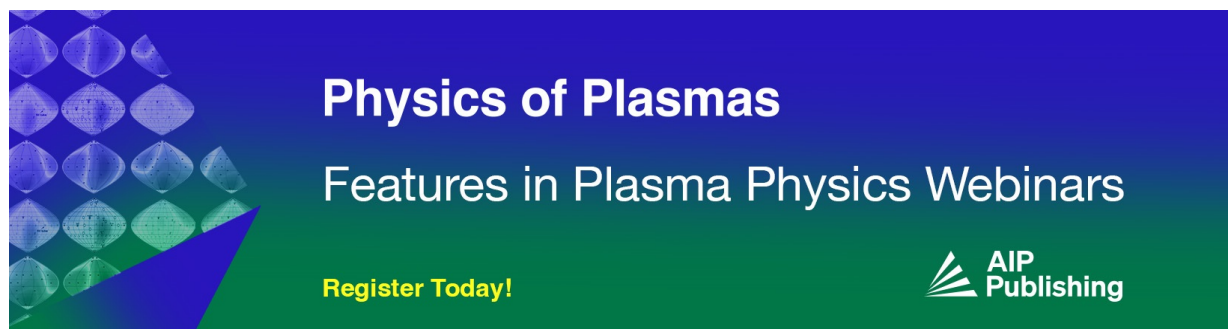Role of hot electrons in mitigating ablative Rayleigh–Taylor instability
Physics of Plasmas 30, 022706 (2023); https://doi.org/10.1063/5.0124462

Intricate structure of the plasma Rayleigh–Taylor instability in shock tubes
Physics of Plasmas 30, 022709 (2023); https://doi.org/10.1063/5.0129149

Toward more robust ignition of inertial fusion targets
Physics of Plasmas 30, 022702 (2023); https://doi.org/10.1063/5.0120732

Physics of Plasmas

Features in Plasma Physics Webinars

Register Today!

AIP Publishing

The effect of collisions on the multi-fluid plasma Richtmyer–Meshkov instability

View Online   Export Citation   CrossMark

K. C. Tapinou,[1,a] V. Wheatley,[1] D. Bond,[1] and I. Jahn[2]

AFFILIATIONS

[1]Centre for Hypersonics, The University of Queensland, Brisbane, QLD 4072, Australia
[2]Institute of Advanced Engineering and Space Sciences, University of Southern Queensland, Toowoomba, QLD 4350, Australia

[a]Author to whom correspondence should be addressed: kyriakos.tapinou@uqconnect.edu.au

ABSTRACT

The Richtmyer–Meshkov instability (RMI) results from the impulsive acceleration of a density interface where the RMI itself or the acceleration is perturbed. The RMI is ubiquitous in shock environments and may arise due to an interface of fluid species, isotopes, temperature, or more. The plasma RMI can be significantly influenced by electromagnetic effects and can be modeled more accurately by a multi-fluid plasma (MFP) model rather than conventional magnetohydrodynamics, though with increased computational expense. MFP modeling of the plasma RMI has revealed many phenomena but has only been completed within the ideal regime. Modeling the effects of elastic collisions is vital for understanding the behavior of the instability in a dense plasma. The Braginskii transport coefficients provide the-oretically based relations modeling thermal equilibration, inter-species drag, viscous momentum- and energy-transfers, and thermal conductivity. Our numerical simulations of the MFP RMI with these relations show that the key changes from the ideal case are (1) reduction of relative motion between the ion and electron fluids (consequently affecting the self-generated electromagnetic fields), (2) introduction of anisotropy in momentum and energy via transport coefficients, and (3) damping of high frequency electromagnetic waves and plasma waves. Under the conditions studied, the net effect is a reduction in the MFP RMI amplitude width and the growth rate to levels approaching the neutral fluid instability, as well as a reduction in large scale perturbations along the ion fluid density interface, a positive for inertial confine-ment fusion efforts. There are, however, two important caveats: small-scale density interface perturbations remain, and the conditions simu-lated are a few relevant points in a large parameter space that requires further investigation.

I. INTRODUCTION

The promise of developing a carbon-neutral and plentiful power source, a solution to many existential crises facing human-ity, has motivated research in thermonuclear fusion for over a generation. Incremental progress toward the goal of net power-generation from fusion has continued steadily, though slowly, with several key milestones passed and others on the near horizon. In the inertial confinement fusion (ICF) branch of fusion efforts, the next key milestone is "ignition," where self-sustaining fusion reac-tions consume all the inertially confined fuel within the target. Recent results at the National Ignition Facility (NIF) have made significant progress toward ignition by achieving a "burning" plasma,[1] releasing more heat from fusion reactions than is input to the fuel target. One of the core issues that must be resolved before achieving ignition is the presence of hydrodynamic instabilities within the fuel target.[2–4]

A review of early ignition experiments found that "Current evi-dence points to low-mode asymmetry and hydrodynamic instability as key areas of research to improve the performance of ignition experi-ments on the NIF and are a central focus of the Ignition Program going forward."[2] The primary hydrodynamic instabilities that affect the fuel capsule during implosion are the Rayleigh–Taylor instability (RTI), the instability of superposed fluids continuously accelerated from the heavy fluid to the light, and the Richtmyer–Meshkov instabil-ity, the impulsive analog of the RTI that is most influential at early time and in the presence of shock-waves that drive the implosion. Much of the effort to suppress the hydrodynamic instabilities has been focused on RTI and to a lesser extent the Richtmyer–Meshkov insta-bility (RMI), via manipulation of the laser pulse characteristics that produce the driving shock-waves.

Extracting telemetry for the parameters of interest within the fuel assembly during experiments is difficult due to the violent and high

energy processes created during an ICF implosion. Even more challenging is the requirement for noninvasive diagnostic techniques that would otherwise exacerbate hydrodynamic instabilities, degrade implosion-symmetry, and disrupt the delicately constructed fuel assembly. The burn-averaged total areal density, neutron-averaged hot-spot ion temperature, and neutron yield are typical measurable quantities.[5] The areal density is a measure of the amount of compression achieved and is a fundamental ICF parameter given from the Lawson criteria.[6,7] Any derived quantities must be related to the few measurable parameters from experiments via the physics of energy confinement and losses, assuming that the existing theories and knowledge of the fuel capsule implosion are well understood. In the absence of abundant and pertinent diagnostic information, research efforts rely on numerical simulations to complement experimental results and provide insight to physical processes occurring within the target.

Modeling methodologies for the plasma RTI and RMI vary widely, and the literature on the plasma RMI is particularly limited. Common modeling approaches are single-fluid reductions with the major multi-physics modeled to capture interactions of phenomena[8,9] or dedicated plasma modeling. The dedicated plasma modeling tend to employ one of the following: the ideal magnetohydrodynamic (MHD) model,[10–14] the Hall magnetohydrodynamic (HMHD) model,[15,16] or the multi-fluid plasma (MFP) model.[17–19] Kinetic models are generally not employed because of their great computational expense. The MFP modeling approach offers an attractive compromise; it possesses a superior grasp of the physics involved compared to the ideal and Hall MHD models that are simplified in their treatment of the physics, but still allows simulations of practical significance compared to kinetic models. The MFP theory captures the key effects of charge separation, Lorentz forces, self-generated electromagnetic (EM) fields, fluid interactions (electron fluid exciting ion fluid), and high frequency phenomena. Importantly, the MFP theory can resolve the differences between the fundamental material interface types present in a plasma RMI which cannot be distinguished by MHD and HMHD due to their simplifications.[19]

The Richtmyer–Meshkov instability (RMI) typically results from the impulsive acceleration of a perturbed density interface. It is unstable in any density interface arrangement and leads to instability growth and produces turbulent mixing. The instability was first identified by Markstein[20] with the first theoretical and experimental characterizations completed by Richtmyer[21] and Meshkov,[22] respectively, who are the instability's namesakes. The RMI is ubiquitous in high-energy environments, and some of the current research on the RMI are motivated by mitigation of hydrodynamic instabilities in ICF,[2–4,18,23–25] enhancing mixing in supersonic combustion,[26,27] many astrophysical phenomena,[28,29] atmospheric sonic boom propagation,[30] driver gas contamination in reflected shock tunnels,[31,32] combustion wave deflagration-to-detonation transition,[33,34] laser–material interactions, including but not limited to microfluid dynamics[35] and micrometer-scale fragment ejection,[36] high energy density turbulent mixing,[25] and many more fundamental studies investigating the solid–liquid and solid–solid media interactions with lasers and fluid flows. The aforementioned list of research areas is by no means complete as the RMI is important in many other natural and engineered formats. A brief and informative review is provided by Brouillette,[37] and detailed reviews are available from Zhou[38] and Zhou et al.[39]

MFP models feature individual sets of conservation laws for ions, neutrals, and electrons, coupled to Maxwell's equations, allowing the modeling of charge separation and the consequent generation and evolution of EM fields that is not possible with single-fluid models. The resulting MFP effects fundamentally alter the evolution and severity of the generic plasma RMI[18] and produces a different RMI evolution for the isotope, species, and thermal density interface cases that are near indistinguishable in the ideal MHD model and other single-fluid models.[19] The key phenomena influencing the plasma RMI are the following:

1. primary Richtmyer–Meshkov instability,
2. electromagnetically driven Rayleigh–Taylor instability,
3. Kelvin–Helmholtz instability,
4. electron-fluid-excitation of the ion–fluid interface,
5. Lorentz force bulk fluid accelerations and vorticity deposition,
6. transverse-reflected shock-wave interaction with the ion–fluid interface, and
7. a multi-fluid plasma shock refraction process.

Points (1), (3), and (6) are observable in the hydrodynamic models of the RMI and MHD reductions of the plasma RMI; however, the remaining phenomena are beyond their grasp because of the required capacity to model self-generated EM fields and the evolution of electron fluid. All three interface types previously studied (isotope, species, and thermal RMI[19]) experience the phenomena above to varying degrees. The isotope case, lacking an initial density interface in the electrons, is the closest to the single-fluid limit. The thermal and species interface scenarios with their initial electron fluid mass density ratios experience significant multi-fluid effects and amplification of the RMI in the larger Debye length cases. As the Debye length is reduced (increasing coupling between the ion and electron fluids), all three novel interface types tested experience a significantly reduced RMI growth rate and amplitude, approaching the single-fluid limit but retain multi-fluid phenomena. The results of previous studies[18,19] show that MFP effects should be considered important when (i) Debye lengths are large enough to permit relative motion between species, and (ii) distinct density interfaces are formed from isotope, species, and thermal discontinuities.

To realistically simulate the evolution of the RMI at plasma conditions relevant to ICF, the ideal MFP model is extended to include collisional effects. Studies investigating ICF implosions show that kinetic effects are significant and required for accurate modeling of the implosion dynamics.[40,41] The Braginskii transport coefficients[42] model the effect of elastic collisions within (intra) and between (inter) species of an ion–electron plasma. Braginskii derived these coefficients beginning from the Boltzmann equation and using the Landau Collision operator. Taking moments of the Boltzmann equation recovers fluid conservation equations with terms representing the influence of the collision operator on the conserved quantities. A two-term Sonine (Laguerre) polynomial is used to approximate the distribution functions—the primary source of numerical inaccuracy is from the truncation of the polynomial terms and the polynomial fit.

The Braginskii[42] transport coefficients relate the thermodynamic properties of the plasma to those of: momentum transfer between the plasma species; the viscous stresses; the heat fluxes; the heat generated due to viscous dissipation; and the thermal equilibration between the species. Braginskii recovers a set of separate transport coefficients for

the electrons and ions with different temperature and velocities that are decoupled. The resulting decoupled equations have an ion distribution with dependence on self-interaction and an electron distribution with a dependence on the self- and cross-interactions. Braginskii's[42] derivation neglects inelastic collisions, ionization, fusion, recombination, rotational degrees of freedom, and the effect of magnetic fields on the Landau collision operator.

The Braginskii transport model has been implemented in varying degrees within plasma simulation codes. Berlok et al.[43] implemented Braginskii viscosity (intra-species terms) in MHD to study weakly collisional plasmas that comprise the intra-cluster medium (ICM) of galaxy clusters, utilizing a second-order accurate Runge–Kutta–Legendre supertime-stepping algorithm to alleviate the viscous time step constraint. Sadler et al.[44] incorporated the model within an MHD formulation motivated by applications in collisional astrophysics and high energy density plasmas. Li and Livescu[45] implement the full-Braginskii transport terms to the multi-fluid plasma equations but then use the infinite speed of light and negligible electron inertia approximations to lessen the stiffness of the system of equations. Srinivasan[17] implemented the Braginskii formulation within a multi-fluid plasma model, neglecting the gyro-viscosity terms for simplicity, and Shumlak et al.[46] utilized the resulting numerical tool to study Z-pinch dynamics (anomalous resistivity and plasma sheath formation) in a field reversed configuration. Meier and Shumlak[47] provide a study of the Z-pinch dynamics utilizing only the intra-species terms, the inter-species terms being neglected because their timescale exceeds the hydrodynamic timescale (characteristic length divided by the Alfvén speed v_A), though the authors include the diamagnetic transport terms introducing some form anisotropy. It is rare that the full-Braginskii transport terms are implemented in true multi-fluid plasma framework due to numerical stiffness and problem specific relevance. Alternative modeling approaches are preferred, notably Miller[48] used a 13-moment fluid model derived from the Pearson type-IV probability distributions to successfully model transition from the collisional to weakly collisional regimes.

The present paper is organized in the following way. Section II outlines the non-dimensionalization, Braginskii transport coefficients, and relevant implementation details. Section III outlines the numerical tool used, non-dimensional initial conditions, and the reference conditions. Section IV presents the test cases for the implementation of the Braginskii transport coefficients. Section V describes the reference cases (the hydrodynamic and ideal MFP case) used to compare to the results with elastic collisions modeled by the Braginskii transport coefficients. Section VI discusses simulation results for the separate cases of intra-species, inter-species, and combined intra- and inter-species elastic collisions (henceforth, we refer to this combined case as the full Braginskii or FB case), where we consider the effects with and without magnetic field induced anisotropy. Section VII focuses on the FB case with anisotropy modeled, investigating the interface statistics and unique features. The conclusion follows in Sec. VIII.

II. METHODOLOGY

This investigation's key objective is the identification and understanding of the effects of elastic collisions on the plasma RMI at conditions relevant to ICF. To this end, the conditions of the investigation are simplified so the influence of other physical phenomena are not conflated with that of the elastic collisions. Consider the "other"

physical phenomena as those associated with radiation transport, laser–surface interactions, multi-phase modeling, shell-dynamics, nuclear reactions, converging geometry, ablation, and the process of ionization. Isolating the RMI in this way reduces problem complexity and simplifies investigative tools and analyses required for the works proposed. Additionally, reducing the computational overhead of multi-physics modeling frees the computational resources on hand to be directed at the far more physically accurate but also more computationally expensive MFP model, relative to ideal and Hall MHD models.

We use the non-dimensionalization of Bond et al.,[49] itself based on the work by Loverich.[50] The variance in magnitudes of floating point numerics is greatly reduced by the non-dimensionalization, which is vital in resolving the disparate fluid and electromagnetic variables within a single system of equations. In the description of the non-dimensionalization below, the ˆ symbol and subscript zero indicate non-dimensional and reference parameters, respectively. The dimensionalization of the problem is set by four reference parameters; we use length (x_0), ion mass (m_0), mass-density (ρ_0), and electron thermal-velocity (u_0). Once non-dimensionalized, the numerical system stiffness is reduced, and the plasma regime is conveniently set by two parameters, the skin depth ($\hat{d}_S$), and the plasma ratio of thermodynamic and magnetic pressure (β),

$$\hat{n} = \frac{n}{\rho_0/m_0}, \quad \hat{m} = \frac{m}{m_0}, \quad \hat{q} = \frac{q}{q_0}, \quad \hat{\rho} = \frac{\rho}{\rho_0},$$

$$\hat{\mathbf{u}} = \frac{\mathbf{u}}{u_0}, \quad \hat{p} = \frac{p}{\rho_0 u_0^2}, \quad \hat{\varepsilon} = \frac{\varepsilon}{\rho_0 u_0^2}, \quad \hat{x} = \frac{x}{x_0},$$

$$\hat{c} = \frac{c}{u_0}, \quad \hat{t} = \frac{t}{x_0/u_0}, \quad \hat{\mathbf{B}} = \frac{\mathbf{B}}{\sqrt{\frac{2\mu_0\rho_0 u_0^2}{\beta}}}, \quad \hat{\mathbf{E}} = \frac{\mathbf{E}}{c\sqrt{\frac{2\mu_0\rho_0 u_0^2}{\beta}}},$$

$$\hat{d}_S = \frac{d_S}{x_0},$$

where n is the number density, m is the particle mass, q is the charge, ρ is mass density, $\mathbf{u}$ is the velocity vector, p is thermodynamic pressure, ε is the thermal and kinetic specific energy, x is a length, c is the speed of light, t is the time, $\mathbf{B}$ is the magnetic field vector, and $\mathbf{E}$ is the electric field vector. Additional variables used in the paper are temperature T, Boltzmann's constant k_B, atomic number of a species Z, ratio of specific heats γ, vacuum permittivity ϵ_0, the permeability of free space μ_0, and the hydrodynamic Mach number of the propagating shock M. From this point forward in the paper, we drop the ˆ symbol for brevity, and all properties are non-dimensional unless otherwise specified.

Braginskii's transport coefficients, representing elastic collisions, are incorporated by adding the relevant flux and source terms to the momentum and energy conservation equations. The non-dimensionalized set of conservation equations for each fluid are

$$\frac{\partial \rho_\alpha}{\partial t} + \nabla \cdot (\rho_\alpha \mathbf{u}_\alpha) = 0, \tag{1a}$$

$$\frac{\partial \rho_\alpha \mathbf{u}_\alpha}{\partial t} + \nabla \cdot (\rho_\alpha \mathbf{u}_\alpha \mathbf{u}_\alpha + p_\alpha \mathbf{I}) \tag{1b}$$

$$= \sqrt{\frac{2}{\beta_0}} \frac{n_\alpha q_\alpha}{d_S} (c\mathbf{E} + \mathbf{u}_\alpha \times \mathbf{B}) - \nabla \cdot \overset{\leftrightarrow}{\Pi}_\alpha + \sum_{\zeta \neq \alpha} \mathbf{R}_{\alpha\zeta}, \tag{1c}$$

and

$$\frac{\partial \varepsilon_\alpha}{\partial t} + \nabla \cdot ((\varepsilon_\alpha + p_\alpha)\mathbf{u}_\alpha) = \sqrt{\frac{2}{\beta_0}} \frac{n_\alpha q_\alpha c}{d_S} \mathbf{E} \cdot \mathbf{u}_\alpha - \nabla \cdot \mathbf{q}_\alpha - \overset{\leftrightarrow}{\Pi}_\alpha : \nabla \mathbf{u}_\alpha$$

$$\times \sum_{\zeta \neq \alpha} \mathbf{R}_{\alpha\zeta} \cdot \mathbf{u}_\alpha + Q_\alpha, \tag{1d}$$

where the $:$ is a double inner product, the subscript $\alpha \in (i, e)$ represents the species modeled, and ζ represents a second species that collides with species α. $\overset{\leftrightarrow}{\Pi}_\alpha$ is the viscous stress tensor, $\overset{\leftrightarrow}{\Pi}_\alpha : \mathbf{u}_\alpha$ is the heat generated due to viscosity, $\mathbf{R}_{\alpha\zeta}$ is the momentum transfer from species α to ζ, Q_α is the thermal equilibration (collisional heat exchange) between the species, and $\mathbf{q}$ is the heat flux. Note that the sign on the $\mathbf{R}_{\alpha\zeta}$ term is negative for ions and positive for electrons, and the expressions for each of the collisional terms are given in Sec. II A.

We define mass-density, pressure, and energy-density by

$$\rho_\alpha = n_\alpha m_\alpha, \quad p_\alpha = n_\alpha k_B T_\alpha, \quad \text{and} \quad \varepsilon_\alpha = \frac{p_\alpha}{\gamma - 1} + \frac{\rho_\alpha |\mathbf{u}_\alpha|^2}{2}. \tag{2}$$

Maxwell's equations govern the evolution of the EM fields and are given in non-dimensional form,

$$\frac{\partial \mathbf{B}}{\partial t} + c\nabla \times \mathbf{E} = 0, \tag{3a}$$

$$\frac{\partial \mathbf{E}}{\partial t} - c\nabla \times \mathbf{B} = -\frac{c}{d_S}\sqrt{\frac{\beta_0}{2}} \sum_\alpha n_\alpha q_\alpha \mathbf{u}_\alpha, \tag{3b}$$

$$c\nabla \cdot \mathbf{E} = \frac{c^2}{d_S}\sqrt{\frac{\beta_0}{2}} \sum_\alpha n_\alpha q_\alpha, \tag{3c}$$

$$\text{and} \quad \nabla \cdot \mathbf{B} = 0. \tag{3d}$$

A. Braginskii transport model

The equations of the Braginksii's transport model[42] approximate the local solution of the kinetic equation for each species. A two-term Sonine (or Laguerre) polynomial is used to approximate the distribution functions. Numerical inaccuracies arise from the truncation of the polynomial terms and the polynomial fit. The fundamental approach is to obtain separate transport coefficients for the electrons and ions with different temperatures and velocities that are decoupled. The resulting equations have (1) ion distribution with dependence on self-interactions and (2) electron distribution with a dependence on the self- and cross interactions. The numerical coefficients that make up the Braginskii transport coefficients are calculated exactly (after the Sonine polynomials are taken to the second term) and reported with rational numbers.

The key assumptions used in the derivation are as follows. General conservation of the collision integral across the moments is taken such that the number of particles, momentum-density, and energy-density are conserved in like species collisions and dissimilar species collisions. The distribution functions of the species take the form of a Maxwellian distribution. All quantities vary slowly in space and in time, i.e., change must be on length scale larger/longer than the mean free path between collisions and slower than the collision time-scale. The dominant terms in the kinetic equations are the collision operators and the magnetic field term. It is assumed the magnetic field

does not affect the collision integral, i.e., the radius of curvature, the Larmor radius, is large compared to the Debye length. The mass ratio of the ions and electrons is small. The difference in the mean velocities of ions and electrons is small compared with the characteristic electron velocity. The derivation neglects the effects of inelastic collisions such as those resulting in ionization, fusion, recombination, excitation/de-excitation of internal degrees of freedom, and the Landau collision operator does not consider the effect of magnetic fields on itself.

The largest error in the approximation of the transport coefficient is in the regime where the product of the cyclotron frequency and the collision timescale is of the first order. These errors can be as great as 10% to 20%.[42] Since Braginskii's seminal work, several authors have revised the calculation of some of the transport coefficients (typically with respect to accuracy or functional form/physical behavior in limits of strong magnetic fields $\omega\tau \to \infty$).[51,52] Some specific constructive criticisms are the (1) over-estimation of advection due to perpendicular resistivity, $\eta_\perp$ in Braginskii's data fits,[52] (2) inaccuracy of β, $\kappa_\perp$, and κ in the range of $0.3 \geq \omega\tau \geq 30$,[51] among others. We continue with the Braginskii result for simplicity and the ubiquitous comparisons available in the literature while acknowledging their accuracy is limited for some parameter regimes though certainly instructive for the fundamental plasma behaviors.

In the following, note that $d_{d,0}$ and $d_{L,0}$ are the non-dimensional reference Debye length and Larmor radius, respectively, and $\hat{n}_0$ is the product of reference number density and reference length cubed $(\hat{n}_0 = n_0 x_0^3)$. The equations that follow are taken from Braginskii[42] and non-dimensionalized according to the reference values specified at the start of Sec. II. The characteristic collision time scales are the ion and electron collision times τ_e and τ_i, given by

$$\tau_e = d_{d,0}^4 \hat{n}_0 \frac{6\sqrt{2}m_e^{1/2}(\pi T_e)^{3/2}}{\ln(\Lambda)n_i Z^2 q_e^4}, \tag{4}$$

$$\tau_i = d_{d,0}^4 \hat{n}_0 \frac{12 m_i^{1/2}(\pi T_i)^{3/2}}{n_i Z^4 q_e^4 \ln(\Lambda)}. \tag{5}$$

The cyclotron frequencies in the ion and electron fluids govern the magnetic influence on collisions and are given by

$$\omega_{c,e} = \frac{q_e B}{m_e} \frac{1}{d_{L,0}}, \tag{6}$$

$$\omega_{c,i} = \frac{q_e Z B}{m_i} \frac{1}{d_{L,0}}. \tag{7}$$

In the following transport coefficients, we will refer to the components parallel and perpendicular to the local magnetic field, and to the diamagnetic terms. The diamagnetic terms generally refer to transport properties that arise due to imbalances in momentum or energy when counter-propagating fluids interact at a common point within their gyro-orbits. The direction of the resulting net momentum or energy change is perpendicular to both the magnetic field and the instigating property, i.e., relative velocity or temperature gradient. The parallel, perpendicular, and diamagnetic terms are denoted by a subscript $\parallel$, $\perp$, and $\wedge$, respectively. It is important to note the equations shown below are all non-dimensional according to the previous non-dimensionalization and the following:

$$\Pi_0 = \rho_0 u_0^2, \quad q_0 = \rho_0 u_0^3, \quad Q_0 = \frac{\rho_0 u_0^3}{x_0}, \quad R_0 = \frac{\rho_0 u_0^2}{x_0},$$

$$\eta_0 = \rho_0 x_0 u_0, \quad \kappa_0 = \frac{u_0 k_B}{x_0^2}, \quad \beta_0^{TU} = \rho_0 u_0^3, \quad \beta_0^{UT} = n_0, \quad (8)$$

$$\alpha_0 = \frac{\rho_0 u_0}{x_0}.$$

1. Inter-species drag forces

The inter-species forces due to friction and temperature gradients—temperature gradients introduce a diamagnetic effect due to the difference in energies of fluid interacting in opposing gyro-orbits—are denoted by subscript "U" and "T," respectively, and are given by

$$\mathbf{R}_U = -\alpha_\parallel \mathbf{u}_\parallel - \alpha_\perp \mathbf{u}_\perp - \alpha_\wedge \mathbf{u}_\wedge, \quad (9)$$

$$\mathbf{R}_T = -\beta_\parallel^{UT} \nabla_\parallel T_e - \beta_\perp^{UT} \nabla_\perp T_e - \beta_\wedge^{UT} \nabla_\wedge T_e, \quad (10)$$

where, $\mathbf{u}$ is the relative velocity between the electron and ion fluids, $\mathbf{u} = \mathbf{u}_e - \mathbf{u}_i$. The thermal force is only dependent on the electron temperature gradient because the relative velocity which sets the rate of collisions between electrons and ions is dominated by the more mobile electrons. The constants and vector definitions of each direction are given as follows:

$$\mathbf{u}_\parallel = \frac{\mathbf{B}}{|B|}\left(\mathbf{u} \cdot \frac{\mathbf{B}}{|B|}\right) \quad \nabla_\parallel T_e = \frac{\mathbf{B}}{|B|}\left(\nabla T_e \cdot \frac{\mathbf{B}}{|B|}\right),$$

$$\mathbf{u}_\perp = \mathbf{u} - \mathbf{u}_\parallel \quad \nabla_\perp T_e = \nabla T_e - \nabla_\parallel T_e,$$

$$\mathbf{u}_\wedge = \frac{\mathbf{B}}{|B|} \times \mathbf{u} \quad \nabla_\wedge T_e = \frac{\mathbf{B}}{|B|} \times \nabla T_e, \quad (11)$$

$$\alpha_\parallel = \rho_e \nu_e \alpha_0, \qquad \beta_\parallel^{UT} = n_e \beta_0,$$

$$\alpha_\perp = \rho_e \nu_e \frac{1 - \alpha_1' x_e^2 + \alpha_0}{\Delta_e}, \quad \beta_\perp^{UT} = n_e \frac{1 - \beta_1' x_e^2 + \beta_0'}{\Delta_e},$$

$$\alpha_\wedge = \rho_e \nu_e x_e \frac{\alpha_2'' x_e^2 + \alpha_0''}{\Delta_e}, \quad \beta_\wedge^{UT} = n_e x_e \frac{\beta_1'' x_e^2 + \beta_0''}{\Delta_e}. \quad (12)$$

Within Eq. (12), $x_e = \omega_{c,e}\tau_e$, and $\Delta_e = x_e^4 + \delta_1 x_e^2 + \delta_0$. The coefficients for a $Z = 1$ plasma are $\alpha_0 = 0.5129$, $\alpha_0' = 6.461$, $\alpha_0' = 1.837$, $\alpha_0'' = 0.7796$, $\delta_0 = 3.7703$, and $\delta_1 = 14.79$. Coefficients for greater atomic numbers are available in Braginskii[42] (the values for $Z = 1$ and $Z = 3$ are utilized in this study). Note that x_e and Δ_e are dimensionless numbers, and the nondimensionalization of frequency and time are inverses, and therefore there is no residual dimensional coefficients.

2. Viscous stress-tensor

The viscous stress tensor is calculated following the approach of Li and Livescu.[45] The strain-rate tensor is calculated in the simulation reference frame and then transformed into the magnetic field aligned reference frame. The viscous stress-tensor is then calculated as per Braginskii's derivation, which assumes the magnetic field aligned reference frame. Finally, the stress-tensor is then transformed back to the simulation reference frame. The strain-rate tensor is given by

$$\overleftrightarrow{\mathbf{W}}_\alpha = \nabla \mathbf{u}_\alpha + (\nabla \mathbf{u}_\alpha)^T - \frac{2}{3}(\nabla \cdot \mathbf{u}_\alpha)\mathbf{I}, \quad (13)$$

where $\mathbf{I}$ is the identity matrix. The rotation matrix is given by Q,

$$Q = \hat{Q} = \begin{bmatrix} -b_y' & -b_x' b_z'' & b_x'' \\ b_x' & -b_y' b_z'' & b_y'' \\ 0 & b_x' b_x'' + b_y' b_y'' & b_z'' \end{bmatrix}. \quad (14)$$

Therefore, the strain-rate tensor in the magnetic field aligned reference frame is given by

$$\overleftrightarrow{W}_s' = Q^T \overleftrightarrow{W}_s Q. \quad (15)$$

Note the entries of the rotation matrix are unitless, formed by the ratio of magnetic field components and the magnetic field magnitude, given by

$$B'' = \frac{1}{|B|}, \quad B' = \frac{1}{\sqrt{B_x^2 + B_y^2}},$$

$$b_x''\prime = B_x B'', \quad b_x' = B_x B',$$

$$b_y'' = B_y B'', \quad b_y' = B_y B', \quad (16)$$

$$b_z'' = B_z B''.$$

The viscous stress tensor in terms of the strain-rate tensor is given by

$$\overleftrightarrow{\Pi}_{0,0}' = -\frac{1}{2}\eta_0\left(\overleftrightarrow{\mathbf{W}}_{0,0}' + \overleftrightarrow{\mathbf{W}}_{1,1}'\right),$$

$$\qquad -\frac{1}{2}\eta_1\left(\overleftrightarrow{\mathbf{W}}_{0,0}' - \overleftrightarrow{\mathbf{W}}_{1,1}'\right) - \eta_3\overleftrightarrow{\mathbf{W}}_{0,1}',$$

$$\overleftrightarrow{\Pi}_{0,1}' = \overleftrightarrow{\Pi}_{1,0}' = -\eta_1\overleftrightarrow{\mathbf{W}}_{0,1}' + \frac{1}{2}\eta_3\left(\overleftrightarrow{\mathbf{W}}_{0,0}' - \overleftrightarrow{\mathbf{W}}_{1,1}'\right),$$

$$\overleftrightarrow{\Pi}_{0,2}' = \overleftrightarrow{\Pi}_{2,0}' = -\eta_2\overleftrightarrow{\mathbf{W}}_{0,2}' - \eta_4\overleftrightarrow{\mathbf{W}}_{1,2}',$$

$$\overleftrightarrow{\Pi}_{1,1}' = -\frac{1}{2}\eta_0\left(\overleftrightarrow{\mathbf{W}}_{0,0}' + \overleftrightarrow{\mathbf{W}}_{1,1}'\right) \qquad (17)$$

$$\qquad -\frac{1}{2}\eta_1\left(\overleftrightarrow{\mathbf{W}}_{1,1}' - \overleftrightarrow{\mathbf{W}}_{0,0}'\right) + \eta_3\overleftrightarrow{\mathbf{W}}_{0,1}',$$

$$\overleftrightarrow{\Pi}_{1,2}' = \overleftrightarrow{\Pi}_{2,1}' = -\eta_2\overleftrightarrow{\mathbf{W}}_{1,2}' + \eta_4\overleftrightarrow{\mathbf{W}}_{0,2}',$$

$$\overleftrightarrow{\Pi}_{2,2}' = -\eta_0\overleftrightarrow{\mathbf{W}}_{2,2}'.$$

The viscous stress tensor in the original reference frame (laboratory frame) is recovered by using the inverse coordinate transform

$$\overleftrightarrow{\Pi}_s = Q\overleftrightarrow{\Pi}_s'Q^T. \quad (18)$$

The viscous coefficients for the electron fluid are

$$\eta_0^e = 0.96 n_e T_e \tau_e, \quad (19)$$

$$\eta_2^e = n_e T_e \tau_e \frac{1.2 x_{e,\eta}^2 + 2.23}{\Delta_{e,\eta}}, \quad (20)$$

$$\eta_1^e = \eta_2(2x_{e,\eta}), \quad (21)$$

$$\eta_4^e = n_e T_e \tau_e \frac{x_{e,\eta}(x_{e,\eta}^2 + 2.38)}{\Delta_{e,\eta}}, \quad (22)$$

$$\text{and } \eta_3^e = \eta_4(2x_{e,\eta}). \quad (23)$$

Note $x_{e,\eta} = \omega_{c,e}\tau_e$ and $\Delta_{e,\eta} = x_{e,\eta}^4 + 13.8x_{e,\eta}^2 + 11.6$ and $\eta_n(2x_{e,\eta})$ represents η_n a function of $2x_{e,\eta}$ rather than $x_{e,\eta}$, and $\Delta_{e,\eta}(2x_{e,\eta}) = (2x_{e,\eta})^4 + 13.8(2x_{e,\eta})^2 + 11.6$. For the ion fluid, we have

$$\eta_0^i = 0.96 n_i T_i \tau_i, \tag{24}$$

$$\eta_2^i = n_i T_i \tau_i \frac{1.2 x_{i,\eta}^2 + 2.23}{\Delta_{i,\eta}}, \tag{25}$$

$$\eta_1^i = \eta_2(2x_{i,\eta}), \tag{26}$$

$$\eta_4^i = n_i T_i \tau_i \frac{x_{i,\eta}(x_{i,\eta}^2 + 2.38)}{\Delta_{i,\eta}}, \tag{27}$$

and

$$\eta_3^i = \eta_4(2x_{i,\eta}), \tag{28}$$

where $x_{i,\eta} = \omega_{c,i}\tau_i$, $\Delta_{i,\eta} = x_{i,\eta}^4 + 4.03 x_{i,\eta}^2 + 2.33$ and the same procedure described for the electron coefficients is followed, in regard to $\eta_n(x_{i,\eta})$.

Each of the viscosity coefficients refer to a particular type of strain-rate relative to the magnetic field. The stress response of the fluid to expansion/compression is proportional to η_0. The diffusion of momentum *across* the magnetic field is proportional to η_2 and η_1. The diamagnetic effect is accounted for by η_3 and η_4. The five coefficients for three physical processes are used to conveniently solve for the stress-tensor. An arbitrary symmetric second-rank tensor with a zero trace in 3D space is represented by five independent elements.[42,53] Note the scaling of these terms shows that when the ion and electron fluid temperatures are of the same magnitude, the ion viscosity is always much greater than the electron viscosity. Therefore, under most conditions, the ion fluid has the greatest influences on the overall plasma viscosity.

If we are not considering the magnetic field effects on the viscous stress tensor—you may neglect the magnetic field's effect by assuming the gyro-viscosity (anisotropic terms) is negligible or when the magnetic field is zero—the viscous stress tensor is given by

$$\overset{\leftrightarrow}{\Pi}_\alpha = -\eta_0 \overset{\leftrightarrow}{\mathbf{W}}_\alpha, \tag{29}$$

where the coefficients are as before, for the electrons and ions.

3. Viscous heating

The heat generated due to intra-species interactions is given by the double inner product of the viscous stress tensor and the tensor formed by the gradient of the velocity vector (or in tensor notation $\nabla \otimes \mathbf{u}$). We give the equivalence between vector and Einstein summation notation in the following:

$$\overset{\leftrightarrow}{\Pi}_{\alpha,i,j} : \nabla \mathbf{u}_\alpha = \sum_i \sum_j \overset{\leftrightarrow}{\Pi}_{\alpha,i,j} \nabla \mathbf{u}_{\alpha,i,j}. \tag{30}$$

4. Intra-species heat flux

Thermal conduction within each species is accounted for through heat flux terms. The electron heat flux has two contributions that are considered, the first is heat flux from thermal conduction, $\mathbf{q}_{T,e}$,

$$\mathbf{q}_{T,e} = \frac{1}{\hat{n}_0}\left(-\kappa_\parallel^e \nabla_\parallel T_e - \kappa_\perp^e \nabla_\perp T_e - \kappa_\wedge^e \nabla_\wedge T_e\right). \tag{31}$$

The second contribution is the heat flux due to relative velocities in electron populations moving from different regions, induced by thermal forces, creating an imbalance in energy flux, $\mathbf{q}_{U,e}$,

$$\mathbf{q}_{U,e} = \beta_\parallel^{TU}\mathbf{u}_\parallel + \beta_\perp^{TU}\mathbf{u}_\perp + \beta_\wedge^{TU}\mathbf{u}_\wedge, \tag{32}$$

where the coefficients are given by

$$\kappa_\parallel^e = \frac{n_e T_e \tau_e}{m_e}\gamma_0 \hat{n}_0, \quad \beta_\parallel^{TU} = \beta_\parallel^{UT} T_e,$$
$$\kappa_\perp^e = \frac{n_e T_e \tau_e}{m_e}\frac{\gamma_1' x_e^2 + \gamma_0'}{\Delta_e}\hat{n}_0, \quad \beta_\perp^{TU} = \beta_\perp^{UT} T_e, \tag{33}$$
$$\kappa_\wedge^e = \frac{n_e T_e \tau_e}{m_e}x_e\frac{\gamma_1'' x_e^2 + \gamma_0''}{\Delta_e}\hat{n}_0, \quad \beta_\wedge^{TU} = \beta_\wedge^{UT} T_e,$$

where the coefficients for a $Z = 1$ plasma are given by $\gamma_0 = 3.1616$, $\gamma_1' = 4.664$, $\gamma_0' = 11.92$, $\gamma_1'' = 5/2$, and $\gamma_0'' = 21.67$, and x_e and Δ_e are as before specified in Sec. II A 1.

The heat flux for the ion species is assumed to be due only to the thermal conduction because the contribution from relative velocity is assumed negligible due to the massive ions assumption. This yields the expression

$$\mathbf{q}_i = \mathbf{q}_{T,i} = \frac{1}{\hat{n}_0}\left(\kappa_{//}^i \nabla_{//} T_i - \kappa_\perp^i \nabla_\perp T_i - \kappa_\wedge^i \nabla_\wedge T_i\right), \tag{34}$$

where the thermal conductivities, κ, are given by

$$\kappa_\parallel^i = 3.906 \frac{n_i T_i \tau_i}{m_i}\hat{n}_0, \tag{35}$$

$$\kappa_\perp^i = \frac{n_i T_i \tau_i}{m_i}\frac{2x_i^2 + 2.645}{\Delta_i}\hat{n}_0, \tag{36}$$

and

$$\kappa_\wedge^i = \frac{n_i T_i \tau_i}{m_i}x_i\left(\frac{\frac{5}{2}x_i^2 + 4.65}{\Delta_i}\hat{n}_0\right), \tag{37}$$

with $x_i = \omega_{c,i}\tau_i$ and $\Delta_i = x_i^4 + 2.70 x_i^2 + 0.677$.

5. Inter-species energy exchange

Inter-species collisions lead to a thermal equilibrium developing between the species. The thermal equilibration is modeled by

$$Q_\Delta = 3\frac{m_e}{m_i}\frac{n_e}{\tau_e}(T_e - T_i). \tag{38}$$

Braginskii[42] assumes the ion–electron friction heating is negligible since it is proportional to $m_{i,e} = \frac{m_i m_e}{m_i + m_e}$. In this paper, the artificially greater mass electrons used for numerical stability mean the contribution to the ion energy equation (consider the mass ratio) is greater than the physical values ($m_i/m_e = 100$ rather than the real $m_i/m_e = 1836$ for hydrogen ions) but still negligible. Therefore, we retain the treatment by Braginskii, which uses conservation of total energy resulting in

$$Q_i = Q_\Delta, \tag{39}$$

$$Q_e = -\mathbf{R}_U \cdot \mathbf{u} - \mathbf{R}_T \cdot \mathbf{u} - Q_\Delta. \tag{40}$$

B. Implementation details

Braginskii transport is for collisional plasmas near thermal equilibrium. It is suitable in the Knudsen number range on the order of $10^{-5} < Kn < 10^{-2}$. Departing from this regime can cause the characteristic properties, i.e., collision time scales to become very large or

small leading to nonphysical transport coefficients. Accordingly, the collision frequencies (non-dimensional) are checked during the simulation to avoid divide by zero errors,

$$\nu = \max(\nu, \varepsilon_{float}), \quad (41)$$

where $\varepsilon_{\text{float}}$ is the effective zero for calculations within the code, usually 1×10^{-14}. In the low collisionality regime, the collision frequency can be set to some minimum characteristic frequency to avoid numerical errors, as recommended by Srinivasan,[17]

$$\nu = \max(\nu, \min(0.1\omega_p, 0.1\omega_c)). \quad (42)$$

Though this is implemented in the code, it is not utilized in our simulations.

III. NUMERICAL SOLVER AND INITIAL CONDITIONS

A. Numerical solver

The numerical implementation used for this work was developed by Bond et al.[18] and is named Cerberus. Cerberus is a finite volume code built in the adaptive mesh refinement (AMR) framework AMReX.[54] Inherited from AMReX is the capacity to simulate massively parallel, block-structured adaptive mesh refinement (AMR) solutions on architectures up to the exascale. Cerberus is capable of three-dimensional simulation though here we use the two-dimensional three-vector architecture. Consequently, these scenarios do not produce x- and y-magnetic field components; however, there is generation of the z-component of magnetic field as well as x- and y-electric fields. The numerical solution requires a very high degree of spatial and temporal refinement due to the small length scales and advective speeds associated with the plasma regime modeled. The spatial refinement is easily satisfied by the AMReX capabilities. The trigger we use for the cell refinement is the relative ion and electron mass density gradient. A threshold value for the gradient is set according to

$$\mathfrak{g} = \frac{v_1 - 2v_0 + v_{-1}}{|v_1 - v_0| + |v_0 - v_{-1}| + 0.01(v_1 + 2v_0 + v_{-1})}, \quad (43)$$

where v is the primitive variable of interest calculated for a centered stencil. The gradient is determined along each spatial dimension of the solution is performed along each dimension. The temporal refinement is satisfied in some part by manipulating the resolved value of speed of light in the non-dimensionalized parameter space. The manipulation is in choosing a large value for the reference velocity so the non-dimensional speed of light, $\hat{c} = c/u_0$, is smaller, thereby lessening the

temporal refinement required by the Courant–Friedrichs–Lewy (CFL) condition than what is typical in most plasmas. Care must be taken to ensure that the non-dimensional speed of light is still the greatest characteristic speed in the system; otherwise, nonphysical behavior due to the interaction of the fluid and EM waves may occur.

The time integration is calculated with a two-stage second-order accurate Runge–Kutta scheme.[55] Linear cell reconstruction is carried out with second-order van Leer limiting.[56] Fluid (ions and electrons) and electromagnetic fluxes are computed with the HLLC[57] and Rankine–Hugoniot[58] solvers. The source terms are calculated via a locally implicit solution of the source terms, according to the method of Abgrall and Kumar.[59] The inviscid flux constraint on time steps is enforced by using 0.5 for the CFL number. The dissipative flux constraint on time is calculated from the spatial scale (Δx) and diffusivity (ν) of the relevant physical process enforced according to

$$\Delta t \le \frac{\Delta x^2}{2\nu}, \quad (44)$$

where $\nu_{\text{diffusion}}$ is given by the physical process, i.e.,

$$\nu_{\text{viscous}} = \frac{\eta}{\rho} \quad \text{and} \quad \nu_{\text{thermal}} = \frac{\kappa}{C_p \rho}, \quad (45)$$

where the cell values of viscosity (η), mass-density, thermal conductivity (κ), and specific heat capacity (c_p) are used to calculate the viscous and thermal diffusivity. Electromagnetic divergence constraints were enforced using a projection method, driven by an elliptical PDE solver. Further details on Cerberus are available in Bond et al.[18]

B. Initial conditions

The generic problem follows that of Bond et al.[18] which was designed to be comparable to previous RMI studies.[10,12,60] Figure 1 shows the initial plasma configuration that forms a three-zone Riemann problem consisting of zones 0 (S_0), 1 (S_1), and 2 (S_2) from the left boundary. The interface between S_0 and S_1 generates a shock that travels to the right where it encounters the interface formed between fluids in region S_1 and S_2. The perturbation of the interface between S_1 and S_2, is chosen to consist of a single period of a sinusoid with an amplitude of 0.1 non-dimensional length ($\frac{1}{10}$ domain width). The perturbation mean location in the x-dimension is 0.2 non-dimensional lengths from the initial shock. The density interface studied in this work is a material interface. The initial interface is a stationary contact discontinuity without any mass or heat flux (we do not consider, for example, the kind that would be involved in the RMI of a
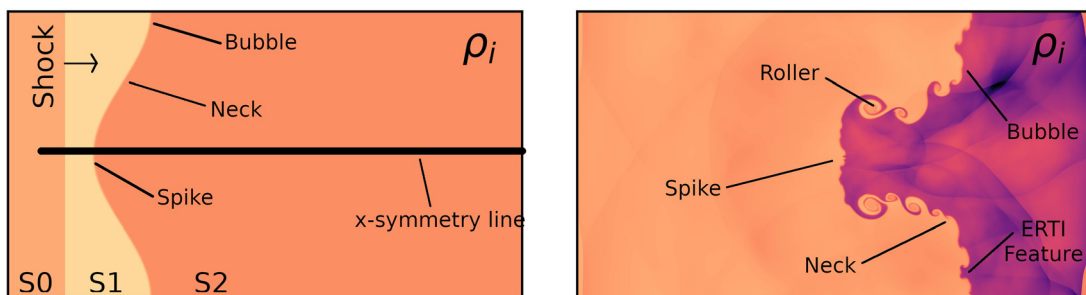

FIG. 1. An example of the initial conditions and developed evolution of the RMI.

traveling flame front). Furthermore, there are no phase changes associated with the interface in this work.

As an initial condition, charge neutrality is enforced everywhere and mechanical equilibrium is enforced between S_1 and S_2 as minimum requirements for initial stability and clarity of results. These two conditions minimize the movement of the interface between S_1 and S_2 prior to the shock interaction due to EM or hydrodynamic effects, excluding the shocks involved in the simulation. The interface is not likely to be stable in actual ICF experiments due to an x-ray preheat preceding the shock, shown to exist in shock tube experiments,[61,62] and drive asymmetries. However, it is useful to model the interface as stable so we may elucidate the fundamental physical phenomena.

The boundary conditions are periodic in the y-dimension and zero gradient in the x-dimension. The domain is taken to be one reference length in the y-dimension, and ± 50 in the x-dimension. The expansive x-dimension of the simulation space is made practical by the adaptive mesh refinement used in the numerical solver, where a very coarse base grid of only eight cells across the domain allows a grid to be inexpensively extended away from the region of interest. The boundary between S_1 and S_2 in Fig. 1 represents the RMI density interface which is chosen to be in the light-to-heavy configuration to avoid complications from a phase inversion (heavy-to-light configuration). A hyperbolic tangent transition function is used between S_1 and S_2 to impose a smooth transition that makes the solution less susceptible to numerical artifacts and to ensure a consistent interface thickness at different resolutions. This function has the form

$$f(x) = f_R + \frac{f_L - f_R}{2}\left(1 + \tanh\left(\frac{2x}{\eta}\operatorname{arctanh}\left[\frac{9f_R - 10f_L}{10(f_L - f_R)}\right]\right)\right), \quad (46)$$

where f_L and f_R are the variable of interest on the left and right of the interface, and η is the width containing 90% of the transition, chosen as 0.01 non-dimensional lengths.

The parameter space in the simulations is large; therefore, a subset must be chosen to make the investigation tractable. The parameters used to define the simulated regime were taken from previous investigations[10,12,19,60] and are the ion fluid species mass-densities either side of the interface, the ion partial pressure for S_1 and S_2, species hydrodynamic and EM properties, e.g., ratio of specific heats and particle charge, and the shock Mach number. Electron fluid parameters, such as fluid mass-densities, pressures, number densities, and temperatures (kT), are set according to the ideal gas equation of state, normal shock relations, and physical properties of the species involved. The following parameters were set:

$$\begin{aligned} m_e &= 0.01, \quad m_{i0} = m_{i1} = 1.0, \quad \rho_{i1} = 1, \\ q_e &= -1.0, \quad q_{i0} = q_{i1} = 1.0, \quad \rho_{i2} = 3, \\ \gamma_e &= 5/3, \quad \gamma_{i0} = \gamma_{i1} = \gamma_{i2} = 5/3, \quad p_{i1} = 0.5, \\ &\text{and} \quad M_0 = 2.0. \end{aligned} \quad (47)$$

The nontrivial relations are the normal shock relations and scalar pressure for a gas obeying a Maxwellian distribution (ideal gas law),

$$\begin{aligned} \rho_{i0} &= \frac{\rho_{i1}}{1 - (2/(\gamma+1))(1 - 1/M_0^2)}, \\ p_{i0} &= p_{i1}\left(1 + \frac{2\gamma}{\gamma+1}(M^2 - 1)\right), \\ p_\alpha &= n_\alpha k T_\alpha, \end{aligned} \quad (48)$$

and the requirements of charge neutrality resulting in the relations

$$\begin{aligned} n_{i0} &= \frac{\rho_{i0}}{m_{^1\text{H}}}, \quad n_{i1} = \frac{\rho_{i1}}{m_{^1\text{H}}}, \quad n_{i2} = \frac{\rho_{i2}}{m_{i2}}, \\ n_{e0} &= n_{i0}Z_{^1\text{H}}, \quad n_{e1} = n_{i1}Z_{^1\text{H}}, \quad n_{e2} = n_{i2}Z_{i2}. \end{aligned} \quad (49)$$

All other parameters are set as a result of those above and the requirements of charge neutrality and mechanical equilibrium. The remaining relations are

$$\begin{aligned} P_{i2} &= P_{i1}, \\ P_{e0} &= P_{i0}, \quad P_{e1} = P_{i1}, \quad P_{e2} = P_{i1}, \\ kT_{i0} &= \frac{P_{i0}}{n_{i0}}, \quad kT_{i1} = \frac{P_{i1}}{n_{i1}}, \quad kT_{i2} = \frac{P_{i2}}{n_{i2}}, \\ kT_{e0} &= \frac{P_{e0}}{n_{i0}Z_{i1}}, \quad kT_{e1} = \frac{P_{e1}}{n_{i1}Z_{i1}}, \quad \text{and} \quad kT_{e2} = \frac{P_{e2}}{n_{i2}Z_{i2}}. \end{aligned} \quad (50)$$

The interface between S_1 and S_2 is set using an interface of hydrogen with a fictitious isotope of lithium, $_3^3\text{Li}$, chosen to match the density ratio from the previous investigation. The scenarios simulated are not accurate quantitative representations of the phenomena occurring in ICF; however, the physical phenomena which are elucidated through these simulations are representative of those which would be exhibited in an ICF experiment. This choice of species is made to elucidate a response from all transport phenomena. The result is a significant ratio across the density interface in the ions and electrons, as well as a temperature interface in the electrons. A summary of the non-dimensional parameters for S_2 is given in Table I.

The temperature discontinuity that results across the density interface is likely to occur in reality. If we consider a non-ionized initial condition with a high enthalpy shock propagating toward the density interface, regardless of having initially constant pressure and/or temperature across the density interface, the result will have non-constant conditions after ionization. Several factors influence the thermodynamic properties of the plasma after the shock interaction and ionization, including the difference in ion and electron number densities from nuclear charge, and ionization energies. To complicate matter, the elements comprising the interface will be ionized by the (1) shock and/or (2) the radiative preheat ahead of the propagating shock (caused by downstream plasma conditions). In either case, there will be non-constant pressure and temperature across the density interface after shock traversal and ionization. If we are instead to consider a situation where the density interface has already been ionized by a preceding shock, then the discontinuity in thermodynamic properties across the shock will depend on the time between successive shock interactions as transport properties across the interface equilibrate properties. Actual experiments will likely experience a plasma RMI of a density interface where there is both pressure and temperature discontinuity, and consequently transport across the interface.

TABLE I. Simulation initial conditions referring to zones displayed in 1.

	m_i	Z_i	ρ_i	T_i	ρ_e	T_e
S_0	1	1	2.29	1.04	2.29×10^{-3}	1.04
S_1	1	1	1	0.5	1×10^{-2}	0.5
S_2	3	3	3	0.5	3×10^{-2}	1.67×10^{-1}

We have chosen to enforce pressure continuity across the interface as an initial condition for numerical convenience and ease of comparison; however, the fundamental effects observed in our simulations for the temperature discontinuity will be present in actual experiments.

Ideally, a single shock-front would be maintained across both fluids until interaction with the density interface. However, the greater sound speed and shock breakdown in the electron fluid mean an electron shock-wave co-incident to the ion shock cannot be produced and maintained after initialization. The resulting general Riemann problem in the electron fluid propagates a single shock and multiple waves. Due to the small Debye length of the simulations (high coupling), the ion and electron shocks propagate at close to the same speed, though with large Debye lengths (loose coupling)[18,19] the electron shock will traverse the interface prior to the arrival of the ion shock.

The volume of fluid tracer quantity used to track the interface is also used to calculate the mixture properties of the ion fluid. The same hyperbolic tangent transition function is used for the tracer as for the conserved properties on the interface, and the tracer has a value varying $\rho \in [0, 1]$ from the left to right states. The single ion fluid modeled in this work is technically a mixture, where the tracer property is equivalent to a mixture fraction. The tracer value is conserved and is convected as a passive scalar. A mixture equation, shown below, is used to find the particle properties when the tracer value is between zero and one. In the following equation, ρ is the tracer value, ϕ is some property, which varies as a linear mixture of the two values,

$$\phi_{\text{effective}} = (1 - \rho)\phi_0 + \rho\phi_1. \qquad (51)$$

Finally, the reference parameters that define the dimension scenario are given in Table II. The reference parameters are in close proximity to ICF experimental values, with the exception of length scale $x_0 = 1 \times 10^{-8}$, giving relevance to the results that follow. The Reynolds numbers characterizing the RMI in the ion and electron fluids (using the reference parameters and total circulation on the interface for the ideal case) are $\text{Re} = \frac{\rho\Gamma}{\mu} = 9$ and 1, respectively, indicating a strong viscous effects within the plasma. The magnetic Reynolds number, Re_m, indicates the relative strength of the advection/induction and diffusion of the magnetic field. Re_m is given by $\text{Re}_m = \mu_0 v_A x_0 / \eta_0$ where v_A is the Alfvén speed, and $\eta_0 = (m_i / q_0 Z \rho_0)(m_e / q_0 \tau_e)$ is the background resistivity and has a reference value of 2.17×10^{-3} for the plasma studied here.

IV. TEST CASES

We investigate several test cases to verify the transport coefficients have been implemented correctly. Previously, the Cerberus code was validated against experimental results for a hydrodynamic RMI (HRMI)[19] and several test cases, such as the plasma shock Bond

et al.[18] Here, we investigate several test exercising the inter- and intra-species transport coefficients.

A. Inter-species elastic collisions

We verify our implementation of Braginskii's elastic collisional terms for inter-species collisions by compared to a similar model, which are presented by Ghosh et al.,[64] and implemented in Cerberus. Comparison of the latter elastic terms implemented in Cerberus with the solutions by Rambo and Procassini[65] is presented by Ghosh et al.[64]

Tests are performed with fully ionized carbon with $q_i = 6$, $m_i = 12$, constant Coulomb logarithm $\ln(\Lambda) = 10$, reference Debye length $d_{D,0} = 2.35 \times 10^{-5}$, and $n_0 = 10^{17}$. Figure 2 shows all the test cases have good agreement with the reference solution by Rambo and Procassini.[65] The first test condition, Fig. 2(a), is computed with ion non-dimensional number densities of $n_A = n_B = 1$ and initial temperatures of $T_A = 1$ and $T_B = 0.25$. We observe both component fluids relax to the equilibrium temperature at the same rate. The second test case, Fig. 2(b), has $n_A = 0.1$, and we observe the fluid temperatures relaxing toward the high-density fluid original temperature. The remaining two cases have fluids with temperatures $T_A = T_B = 0.5$ and x-velocity of $u_A = 2.115$ but either $n_A = n_B = 1$, Fig. 2(c), or $n_A = 0.1$ and $n_B = 1$, Fig. 2(d). In the case of equal densities, both fluids relax toward the equilibrium temperature in the same way, as expected. When the fluids have unequal densities, the less dense fluid is heated due to momentum transfer as it is slowed by impact with the stationary fluid before thermal equilibration due to energy transfer.

We now proceed to comparing the Braginskii transport coefficients with the Cerberus implementation of the model from Ghosh et al.[64] We test a scenario where a stream of ions interacts with background electrons, neglecting Lorentz forces as above.

The first test condition, Fig. 3(a), is with equal non-dimensional number densities of $n_i = n_e = 1$, initial temperatures of $T_i = 1$ and $T_e = 0.25$, and ion x-velocity of $u_i = 2.115$. We see the two fluids equilibrate to the same temperature, slowly as before. The Braginskii formulation thermalizes slower than the Cerberus implementation of model by Ghosh et al.[64] This difference is due to a different expression for the inter-species drag term. In the second case, the ion number density is reduced to $n_i = 0.1$, and the other properties are as before. The difference between the Ghosh and Braginskii implementations is one of the coefficients comprising the momentum drag terms that is different between the two models. Regardless of the small deviation, the model implementations agree well qualitatively and reasonably well quantitatively.

TABLE II. Comparison of typical ICF parameter orders of magnitude,[7] parameters from a single point along an ICF capsule implosion,[63] and those simulated in the present work. In the present work, the reference length is $x_0 = 1 \times 10^{-8}$.

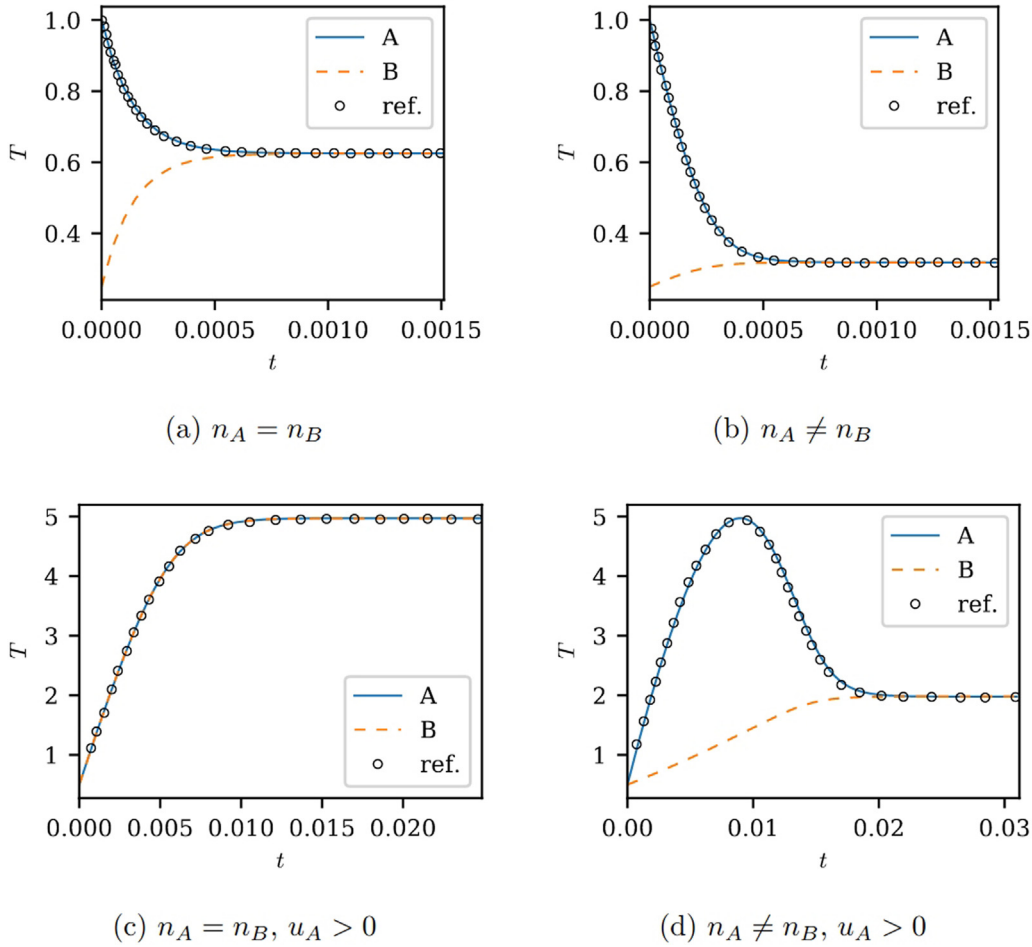|	T (K)	ρ (kg/m³)	d_S (m)	n (m⁻³)	U_{shock} (m/s)
ICF generic	10^6	10^5	10^{-10}	10^{32}	10^5
	10^7	10^4	10^{-9}	10^{31}	
Point on predicted ICF implosion path	3×10^5	1.6×10^4	2.4×10^{-9}	4.7×10^{30}	4×10^5
Current simulation, $\hat{c} = 2000$, $\hat{d}_{S,0} = 7.2$, $\hat{\beta}_0 = 1$	1×10^6	1.6×10^4	1×10^{-9}	1×10^{31}	1.5×10^5

FIG. 2. Comparison of the inter-species elastic collisional terms implemented in Cerberus to the results presented by Ghosh *et al.*[64] (a) $n_A = n_B = 1$ and initial temperatures of $T_A = 1$ and $T_B = 0.25$, (b) $n_A = 0.1$, $n_B = 1$, and initial temperatures of $T_A = 1$ and $T_B = 0.25$, (c) $n_A = n_B = 1$, initial temperatures of $T_A = T_B = 0.5$, and x-velocity of $u_A = 2.115$, and (d) $n_A = 0.1$, $n_B = 1$, initial temperatures of $T_A = T_B = 0.5$, and x-velocity of $u_A = 2.115$.

B. Hartmann flow

The Hartmann flow problem is a useful test case for magneto-viscous and resistive plasmas.[66] We use this test to study the viscous effects and subsequent magnetic field generation in the MFP system forming an ion–electron plasma. The problem resembles a Couette flow, where two parallel plates move longitudinally in opposite directions driving a shear flow along the y-direction. The shear flow in the y-direction, in combination with an imposed x-magnetic field, induces a flow in the z-direction that is balanced by resistive forces. The induced z-direction flow interacts with the imposed x-magnetic field to suppress the y-direction flow.

In deriving analytical solutions, we follow the prescription of Miller[48] and work with the system of equations presented in Sec. II. The problem is two-dimensional and uses the assumptions of slab geometry ($\partial\phi/\partial z = \partial\phi/\partial y = 0$ for any property ϕ), incompressible flow, steady state conditions, no slip, and adiabatic walls (plates) to simplify the governing equations. The assumptions are applied to the system of equations, focusing on conservation of momentum and

substituting the simplified conservation of mass and Maxwell equations, to reduce the problem to the following equations:

$$\frac{\partial^2 u_y^\alpha}{\partial x^2} = -\lambda^\alpha u_z^\alpha + \gamma^\alpha\left(u_y^\alpha - u_y^\beta\right) \tag{52}$$

and

$$\frac{\partial^2 u_z^\alpha}{\partial x^2} = -\lambda^\alpha u_y^\alpha + \gamma^\alpha\left(u_z^\alpha - u_z^\beta\right). \tag{53}$$

Here, we have

$$a_\parallel = \frac{m_e n_e a_0}{\tau_e},$$
$$\gamma_{e,i} = a_\parallel/\eta_{e,0}, \quad \gamma_{i,e} = a_\parallel/\eta_{i,0}, \tag{54}$$
$$\lambda_e = \sqrt{\frac{2}{\beta}\frac{n_e q_e}{d_S \eta_{e,0}}}Bx, \quad \text{and} \quad \lambda_i = \sqrt{\frac{2}{\beta}\frac{n_i q_i}{d_S \eta_{i,0}}}Bx.$$

The reduced equations are solved by assembling a matrix equation of the form $U'' = AU$ with a change of variables. We first perform
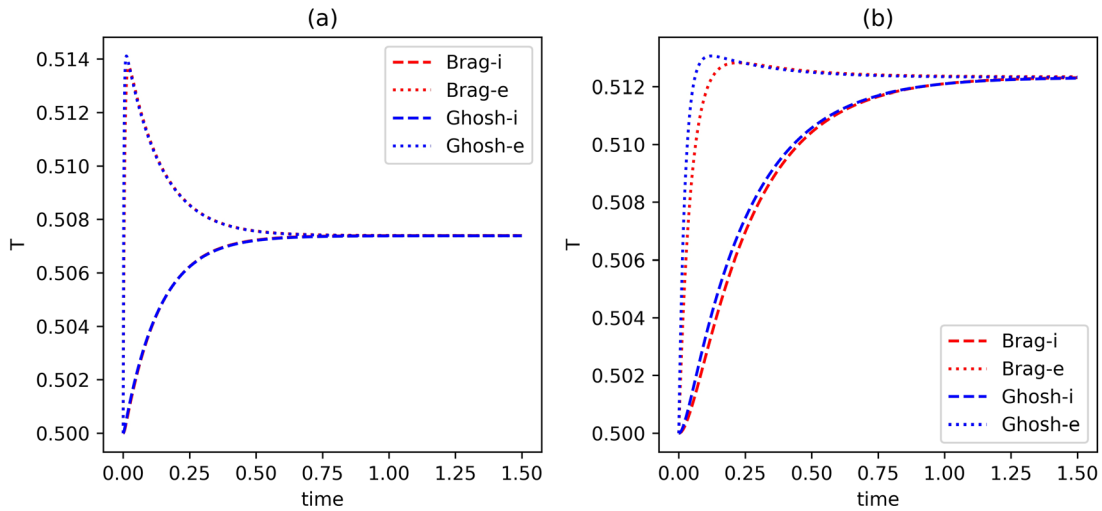
FIG. 3. Comparison of the implementation of the Braginskii transport inter-species elastic collisional terms with the Cerberus implementation of the model presented by Ghosh et al.[64] (a) $n_i = n_e = 1$ and initial temperatures of $T_i = 1$ and $T_e = 0.25$. The Braginskii formulation thermalizes slower than the implementation of Ghosh et al.,[64] due to a different expression for the inter-species drag term. (b) $n_i = 0.1$, $n_e = 1$, and initial temperatures of $T_i = 1$ and $T_e = 0.25$. The difference between the Ghosh and Braginskii implementations is due a different coefficient comprising the momentum drag term.

eigendecomposition of the coefficient matrix, $A = R \cdot D \cdot R^{-1}$, such that $U'' = R \cdot D \cdot R^{-1}U$. If we take an eigenspace velocity to be defined as $S = S = R^{-1}U$, the problem is now recast as an orthogonal equation set $S'' = DS$ where D is a diagonal eigenvalue matrix. The components of S must therefore obey the boundary value problem $S''_i = D_iS_i$ with general solution

$$s_i(x) = C_i^0 e^{\sqrt{D_i}x} + C_i^1 e^{-\sqrt{D_i}x}, \tag{55}$$

where the boundary conditions are $u_y^\alpha(x_l) = -V$, $u_y^\alpha(x_r) = V$, and $u_z^\alpha(x_l) = u_z^\alpha(x_r) = 0$. Solving for the coefficients C_i^0 and C_i^1 is analytically challenging due to the complex nature of the system; therefore, numerical methods are used. The general solution for velocity profiles

is found from changing variables back to the primitives. The magnetic field profiles are found from the steady state Ampère's law integrated in space and enforcing flux conservation.

Cerberus was compared against the analytical solution described above for non-dimensional parameters of

$$V = 1 \times 10^{-3}, \quad B_x = 1, \quad n_i = n_e = 1, \tag{56}$$

$$T_i = T_e = 1, \quad m_i = 1, \quad \text{and} \quad m_e = 1/100. \tag{57}$$

Good agreement was found for the conditions tested and is shown in Fig. 4. Note that the difference in the extreme x values is due to the absence of the ghost cells—the no-slip condition is enforced with ghost
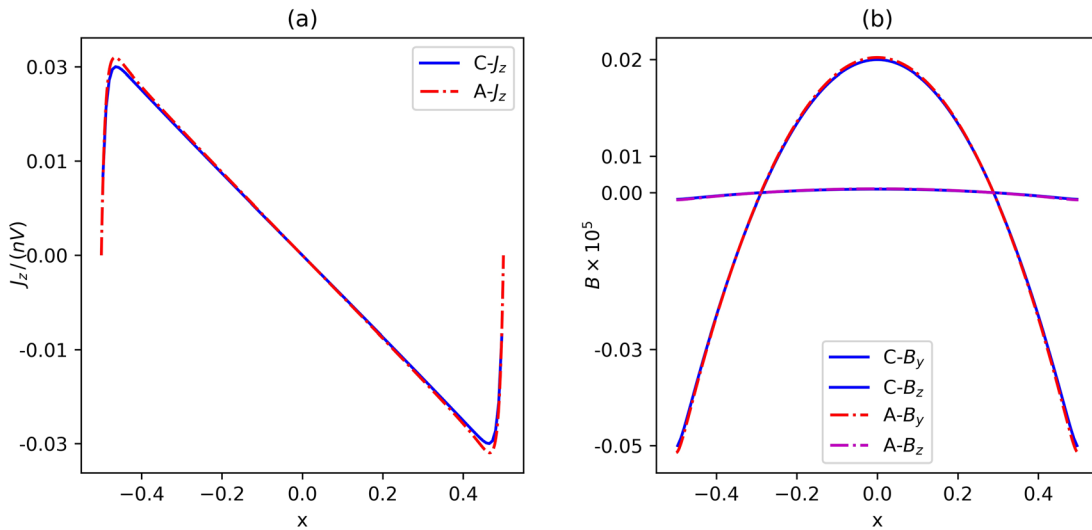

FIG. 4. Cerberus solution compared to the analytic solution for the Hartmann flow test case. The prefixes "C-" and "A-" represent the Cerberus and analytical solutions, respectively. (a) Current density profile that is normalized by the product of reference number density and reference velocity and (b) magnetic field profile.
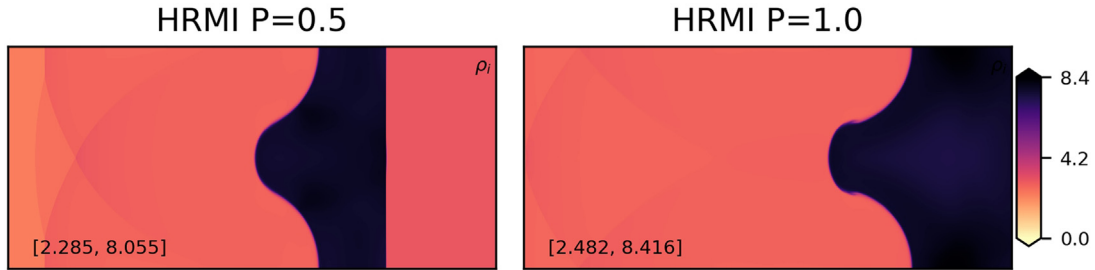
FIG. 5. Hydrodynamic RMI (HRMI) reference solution at simulation end time. The ion mass density, ρ_i, is plotted for both the $P = 0.5$ and $P = 1.0$ reference cases.

cells, making the zero velocity point (and therefore, current density) on the domain boundary.

V. THE IDEAL AND HYDRODYNAMIC REFERENCE CASES

The analogous single-fluid hydrodynamic simulations are provided as part of the reference simulations for comparison to the new collisional MFP RMI simulations. Note the *Braginskii transport coefficients are not modeled in the hydrodynamic simulation*. In the absence of an applied magnetic field, single-fluid hydrodynamic and ideal MHD simulations are identical (when the same density ratio is used). We provide two reference cases for the single-fluid hydrodynamic scenarios, pressures of $p = 1$ and $p = 0.5$. In the case of very loose coupling, the ion and electron fluids are permitted to experience large
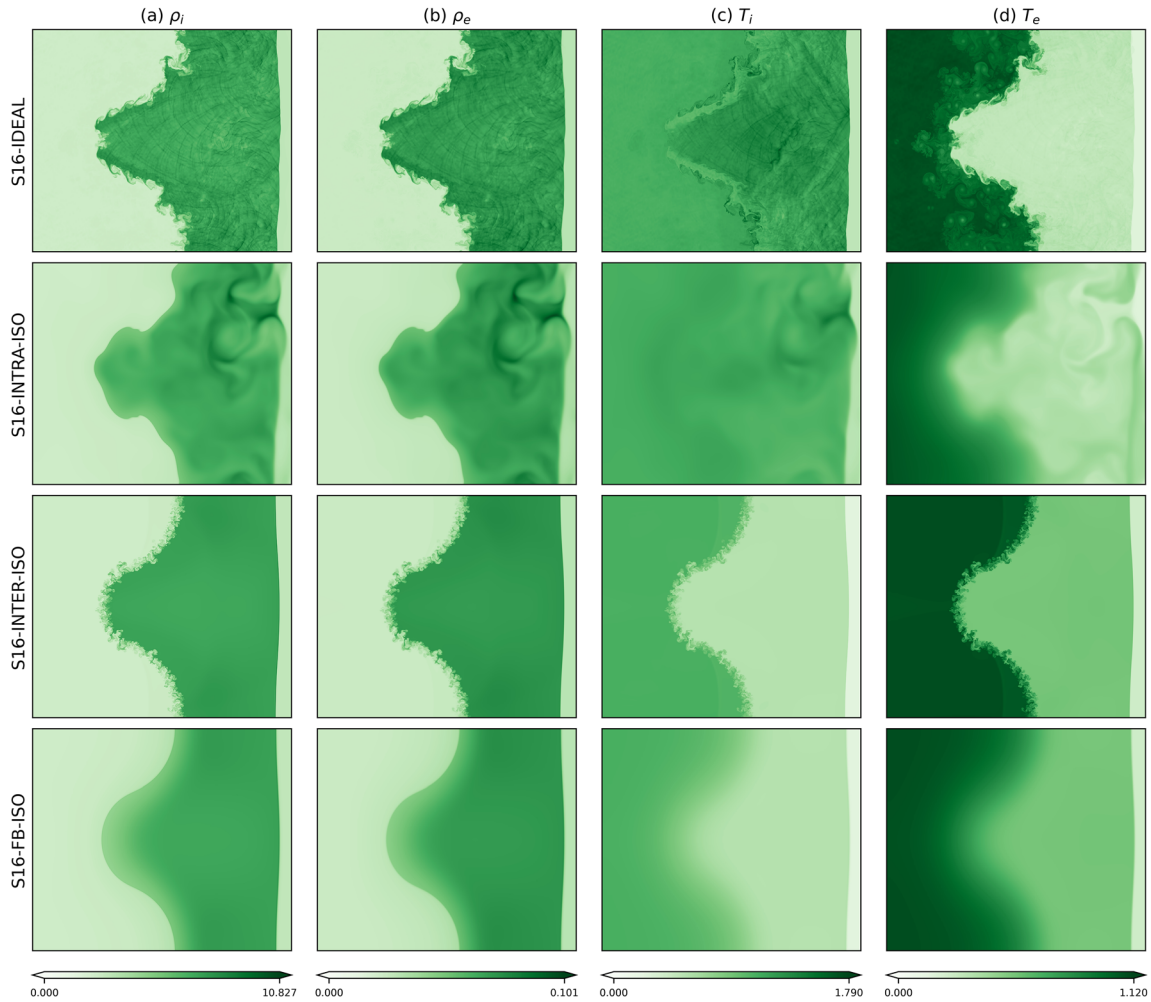
FIG. 6. Final time mass-density and temperature contours (electron and ion) for ideal, intra-species, inter-species, and full Braginskii cases with isotropic transport coefficients.

relative motions and act as if almost independent from each other; thus, the partial pressure of 0.5 in the single fluid case is an appropriate comparison to large skin depths. In the case of very tight coupling, the converse is true, and the two fluids behave as one; thus, a partial pressure of one in the hydrodynamic case is the most appropriate comparison for small skin depth cases. In this manner, the $p = 1$ and $p = 0.5$ hydrodynamic results create an envelope of theoretically expected behavior for the RMI in the ion fluid. The final time mass-density and temperature contours for these cases are shown in Fig. 5.

Moving to the MFP RMI, our reference case is the "ideal" MFP solution, where collisions are absent from the model. Notably, this solution has many more flow features present (Fig. 6 row "S16-IDEAL"). The final time contour plots show a highly perturbed

density interface, shock laden region behind the transmitted shock, strong lateral flows behind the density interface (facilitated by the periodic boundaries), and an early time suction effect pulling fluid through the density interface at the spike. A full analysis of comparable ideal MFP RMI is provided in Bond et al.[18] and Tapinou et al.[19]

Figure 7 shows interface statistics that aid in understanding the evolution of the RMI and secondary instabilities. When interpreting the results of the two-dimensional cases, terminology introduced in Fig. 1 is used: (1) whenever the y-dimension is discussed in the context of the density interface, the lower x-symmetry plane is considered (where positive and negative vorticity will destabilize and stabilize the RMI, respectively, on the lower x-symmetry plane), (2) the "spike" refers to a region of high density fluid penetrating lower density,
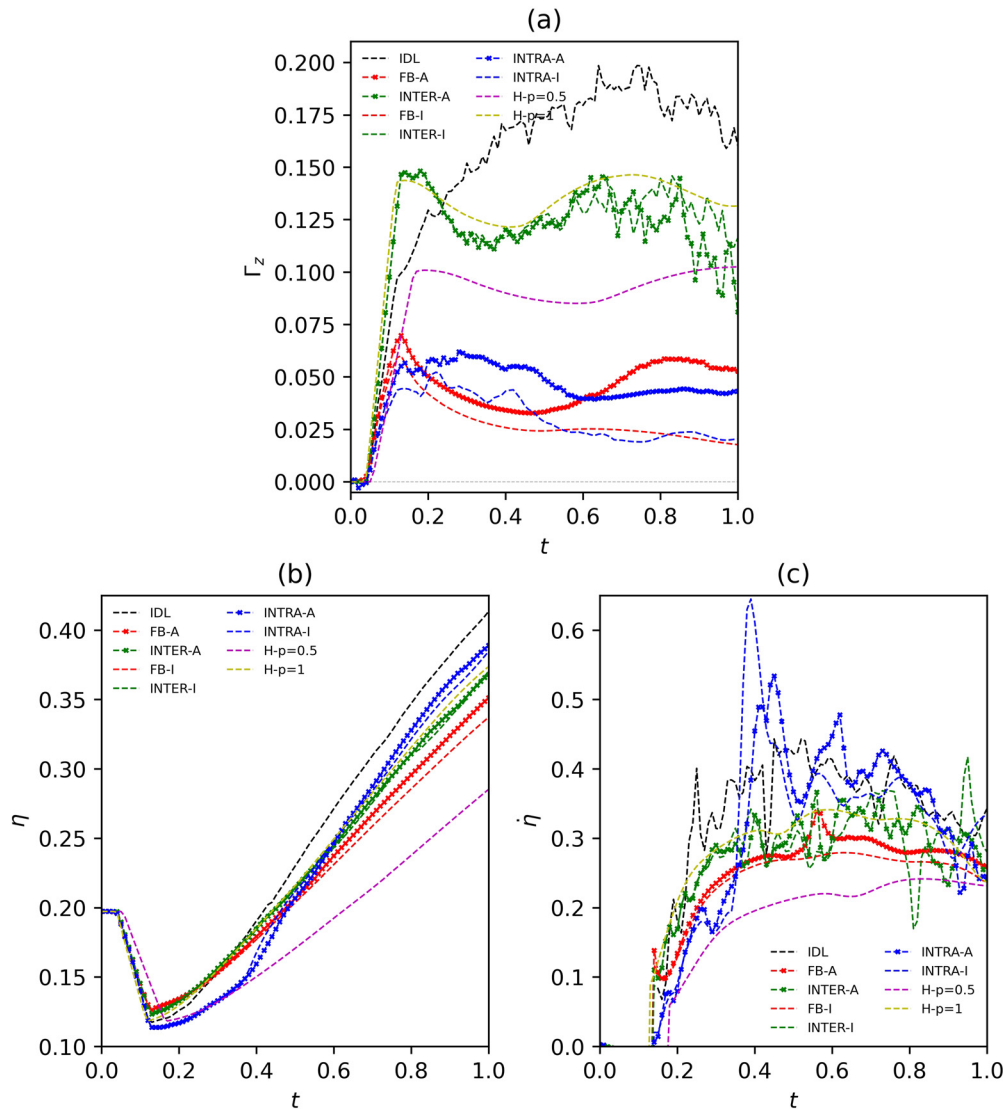

FIG. 7. Interface statistics for the ion fluid in the cases simulated. In the legend labels, "IDL" refers to the ideal case, "INTRA" and "INTER" refer to the intra-species and inter-species cases, respectively, the appended "A" and "I" refers to the anisotropic and isotropic cases, respectively, and the "H" refers to the hydrodynamic cases for pressures of 0.5 and 1, respectively. (a) Accumulated circulation over half-plane, (b) perturbation width, and (c) perturbation width growth rate.
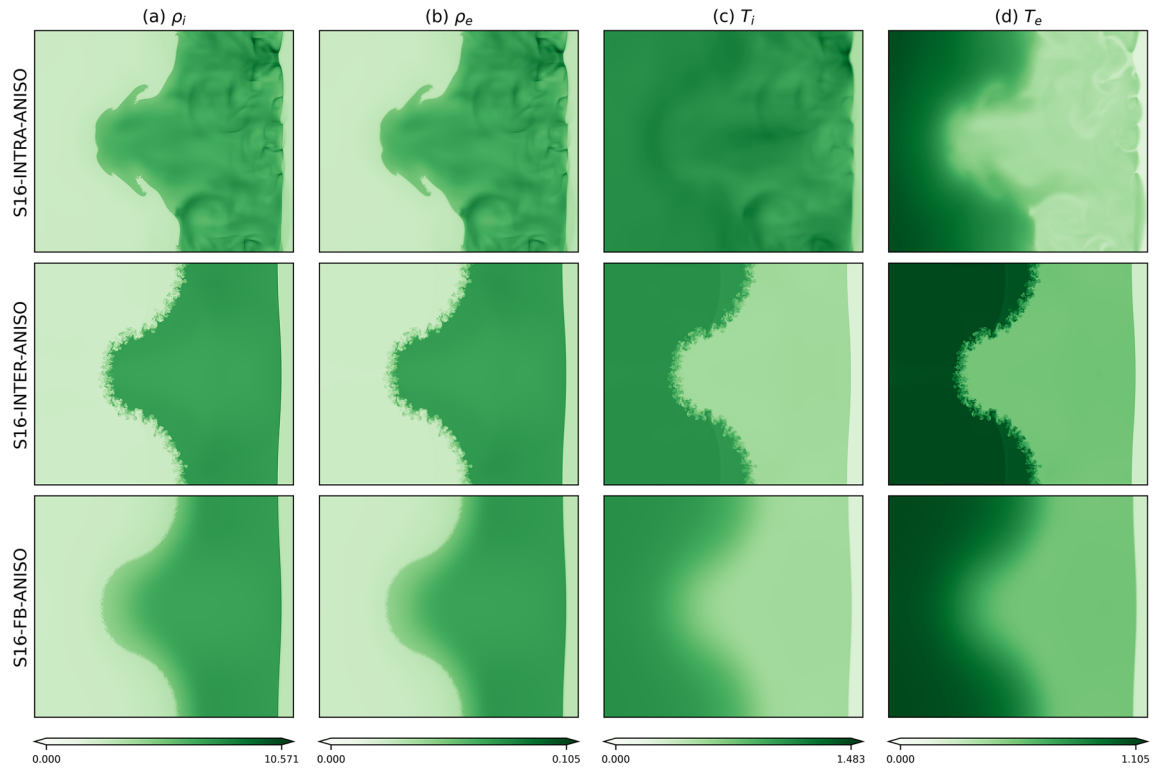
FIG. 8. Final time mass-density and temperature contours (electron and ion) for ideal, intra-species, inter-species, and full Braginskii cases with anisotropic transport coefficients.

(3) the opposite case to point 2 is referred to as a "bubble," (4) the region transitioning between the spike and bubble is referred to as the "neck," and (5) the bottom left numbers within brackets on contour plots are the minimum and maximum values for the quantity of in that figure.

    The interface statistics used are the circulation (Γ_z, on a half period of the interface), generation of circulation ($\dot{\Gamma}_{Z,\text{total}}$, total), and the ion fluid density interface amplitude width (η) and growth rate ($\dot{\eta}$). The vorticity equation is

$$\frac{D\boldsymbol{\omega}}{Dt} = (\boldsymbol{\omega} \cdot \nabla)\mathbf{u} - \boldsymbol{\omega}(\nabla \cdot \mathbf{u}) + \frac{1}{\rho_\alpha^2}(\nabla\rho_\alpha \times \nabla p_\alpha)$$
$$+ \nabla \times \left(\sqrt{\frac{2}{\beta}} \frac{q_\alpha}{d_S m_\alpha}(c\mathbf{E} + \mathbf{u}_\alpha \times \mathbf{B}) \right)$$
$$+ \nabla \times \left(\frac{1}{\rho_\alpha} \left(\nabla \cdot \overset{\leftrightarrow}{\Pi}_\alpha + \sum_{\zeta \neq \alpha} \mathbf{R}_{\alpha\zeta} \right) \right) \quad (58)$$

shows the terms that combine to describe the evolution of vorticity. The terms from the left to the right are the effect of stretching/tilting due to velocity gradients (zero in the z-dimension for 2D), stretching due to flow compressibility ($\dot{\Gamma}_{comp}$), baroclinic generation ($\dot{\Gamma}_{baro}$) that is the primary driver of RMI growth, the electric ($\dot{\Gamma}_{L,E}$) and magnetic field ($\dot{\Gamma}_{L,B}$) torques, and viscous dissipation ($\dot{\Gamma}_{visc}$), and inter-species drag exchange terms ($\dot{\Gamma}_{drag}$). The viscous terms dissipate vorticity and the inter-species collisional terms exchange vorticity between species. The vorticity is related to circulation by

$$\frac{\partial\Gamma}{\partial t} = \frac{\partial}{\partial t}\iint \vec{\omega} \cdot d\vec{S} = \iint \frac{\partial\vec{\omega}}{\partial t} \cdot d\vec{S}. \quad (59)$$

    For an infinitesimal finite area in the x-y plane, we have $\frac{\partial\Gamma_Z}{\partial t} = dA\frac{\partial\omega_z}{\partial t}$, where dA is the area of fluid enclosed by a loop with vorticity. If we take a cell to be the area enclosed by the enclosing loop, we can estimate the instantaneous circulation generated by multiplying terms from Eq. (58) by the area of a cell. Summing the contributions from the cells that comprise the interface is how the instantaneous circulation generation terms are calculated. Likewise, the circulation is found from the sum of vorticity multiplied by cell area for all cells comprising the interface:

$$\frac{\partial\Gamma_Z}{\partial t} = \sum_i A_i \frac{\partial\omega_Z}{\partial t} \quad \text{for} \quad i \in \text{interface cells}, \quad (60)$$

$$\Gamma_Z = \sum_i A_i\omega_{Z,i} \quad \text{for} \quad i \in \text{interface cells}. \quad (61)$$

TABLE III. Final time amplitude width of the primary RMI perturbation. The amplitude is measured using the y-averaged tracer value according to Eq. (62).

		Intra-species		Inter-species		Full-Braginskii	
	Ideal	Iso	Aniso	Iso	Aniso	Iso	Aniso
η	0.41	0.385	0.39	0.37	0.37	0.34	0.35

The interface cells are determined by a heuristic based on the volume of fluid tracer, ρ, value that is convected with the flow. The threshold of tracer value in the x-direction, $[0.05, 0.95]$, is used to establish a preliminary search area. The fluid mass-density gradient and charge density are then used to establish the final interface region, accounting for hydrodynamic and electromagnetic sources of circulation, respectively. The peak of mass-density gradient magnitude in the preliminary search area is used to expand the preliminary region based on the location of the peak. The same procedure is followed for the charge density, and threshold values of 5% of the peak density gradient and charge density are used to establish a final density interface region, for a discrete y-dimension position. This procedure is followed for each discrete y-dimension position until the entire interface region

identified. We note that while this heuristic is useful in finding contributions of terms affecting the rate of change of circulation, it is imperfect. It is used as an indicator of behavior, not an accurate quantitative metric.

The interface width is calculated from the tracer average across the y-dimension where the X coordinates of $\rho_y \in [0.05, 0.95]$ define the interface width,

$$\rho_y = \frac{\int \rho \, dy}{\int dy}. \tag{62}$$

The maximum and minimum transition points are then used to define the interface width and a numerical derivative in time is used to find the growth rate of the interface.
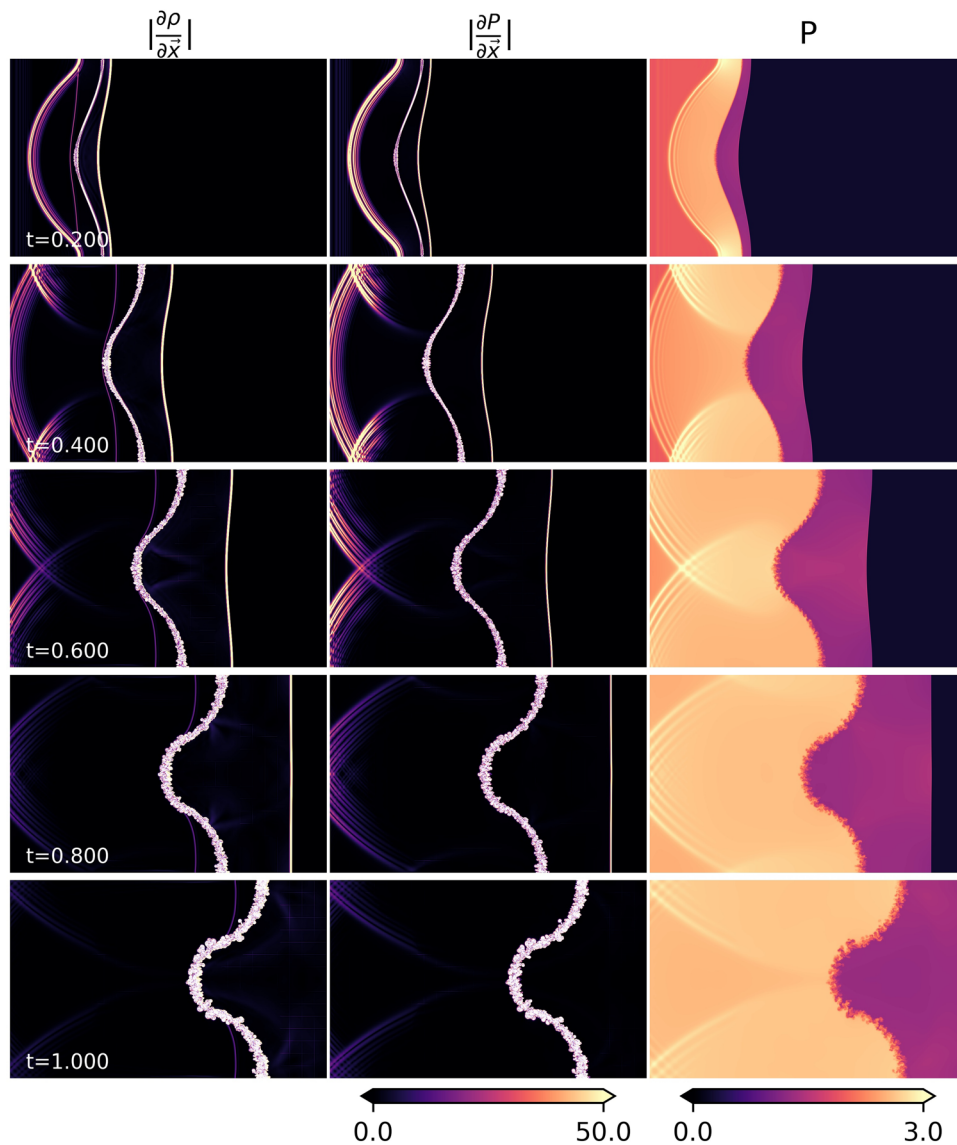

FIG. 9. Contour plots for the inter-species isotropic case showing the gradients in pressure and density, as well as the pressure, for various times.

VI. MFP RMI WITH BRAGINSKII TRANSPORT

The presence of elastic collisions dramatically stabilizes the interface evolution. In comparison to the collisional cases, Fig. 7, the ideal case experiences the most significant RMI and secondary instabilities by measures of amplitude width, amplitude growth rate, and surface perturbations (Figs. 6 and 8). All simulations with collisions produce a significantly reduced amplitude growth, see Table III, compared to the ideal case. The electromagnetically driven RTI (ERTI) is the most significant secondary instability present after shock traversal by way of circulation generation. Previous work[18,19] has shown the importance of the electron fluid's interaction with the ion fluid. The relative motion between the two fluids is vital in generating electromagnetic fields that can enhance the secondary instabilities and also perturb the ion fluid density interface. The incorporation of collisions appears to dramatically reduce the (1) relative motion between the species in the case of inter-species collisions and (2) significantly dissipates the waves and high-wave number disturbances in the intra-species collisional case. The result is a suppression of the ERTI acting on the primary mode perturbation and an inhibition of low-wave number interface perturbation mechanisms.

Comparing the first and second rows of Fig. 6, we see that the intra-species collisions significantly dissipate many of the features observed in the ideal case but permits appreciable RMI growth. The intra-species cases exhibit significant electromagnetic fields around the density interface, a consequence of significant relative motion, which will be explored in Sec. VII. All scenarios simulated have the same level of electromagnetic coupling, so that a disturbance in the electrons is imprinted on the ions (and vice versa) by way of the Lorentz force. In this way, any electromagnetic fields that evolve will influence the ions and electrons. The fields that are evolved in the ideal and intra-species cases (discussed in more detail later in this section), Fig. 13, vary in complicated patterns across the ion and electron fluid density interfaces, thereby seeding perturbations at points of alternating sign and intensity. The perturbations are then amplified by continuous deposition of vorticity through baroclinic and electromagnetic sources driving their growth. The intra-species RMI dissipates most of the small scale features seen in the ideal case whilst allowing some characteristic mushrooming and EM seeded features to develop.

Comparing rows 1 and 3 in Fig. 6, the inter-species collisions are seen to dramatically change the MFP RMI, suppressing the instability of the primary mode far more strongly than the intra-species collisions. As described in the case of the intra-species collisions, points surrounded by alternating EM fields can seed perturbations. In the inter-species case, the mostly homogeneously signed EM fields along the interface removes this mechanism except at the spike and bubble where small perturbations are seeded. Driven by EM interface acceleration, these initially very small perturbations are permitted to grow by the absent viscosity and act as heterogeneous growth points. The perturbation's growth disturbs the EM fields in its surrounding region, seeding perturbations adjacent to it. Figure 9 shows the trail of perturbations emanating from the spike and bubble growing in time. This effect does not occur in the intra-species or full-Braginskii case as the initial small scale perturbations are dissipated before they can grow and seed adjacent perturbations, generating the instability observed here. The inter-species density interface perturbation mechanism is characteristically different in terms of origin, evolution, and physical form. The ERTI of the primary small wave number perturbation is

therefore suppressed while high-wave number perturbations grow instead.

Comparing the bottom row of Fig. 6 to the others, we find that the plasma RMI is suppressed by the full-Braginskii terms and evolves similarly to the hydrodynamic reference solutions with the exception of a unique perturbation mechanism. The packets of transverse reflected waves, clearly visible in the inter-species case, have coalesced into a single diffuse wave front similar to the intra-species case, that is difficult to observe. The full-Braginskii case appears to inherit all of the stabilizing effects present in the preceding cases; consequently, the density interface amplitude and the growth rate are the lowest out of all cases studied. The ion and electron density interfaces are, however, subject to an apparent dual-layer instability (DLI). The combination of inter- and intra-species collisional terms produces a dual-layer—a dual-layer is structure composed of parallel layers of opposite charge-density—between the density interfaces, see Fig. 10. The current densities on the dual-layer initiate an instability that culminates in high-wave number features, resembling filaments emerging from the surface and contorted by the electromagnetic fields. Despite the small scale of these resulting perturbations (see Fig. 8), their effect on shock transmission may be of interest, given the resulting charge distribution and inhomogeneous character along the density interface.

Figure 11 demonstrates how significantly the collisional terms can influence the momentum and energy conservation equations. The primitive variables from the ideal MFP RMI reference case are used to calculate the transport coefficients post-simulation and their contribution to the conservation equations is shown in the contour plots. Immediately obvious from the figures is the dominating effect of inter-species collisional terms on the conservation equations (note the different scales used). The cases that we investigate experience a high thermal equilibration effect because of the initial temperature difference between the ions and electrons in zone 2, a result of enforcing initial charge neutrality and mechanical equilibrium. Generally, the Braginskii transport coefficients in the intra- and inter-species terms vary directly and inversely with the collision timescale, respectively. Since this number is typically small, the inter-species collision terms tend to greater magnitudes but are also dependent on other properties. Figure 12 shows the influence of the transport coefficients in the full-Braginskii case, where these values are actually applied during the simulation run. The magnitudes are much smaller than in the preceding ideal case, simply because the ideal case allows relative magnitudes
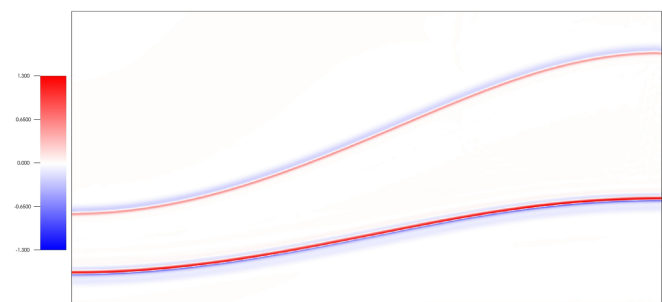

FIG. 10. The dual-layer in charge density at $t = 0.2$, after shock processing of the interface. The lower half of the primary perturbation is shown, with the interface dual-layer (top) and the ion and electron transmitted shocks (bottom) traveling in the positive x-direction (down the figure).
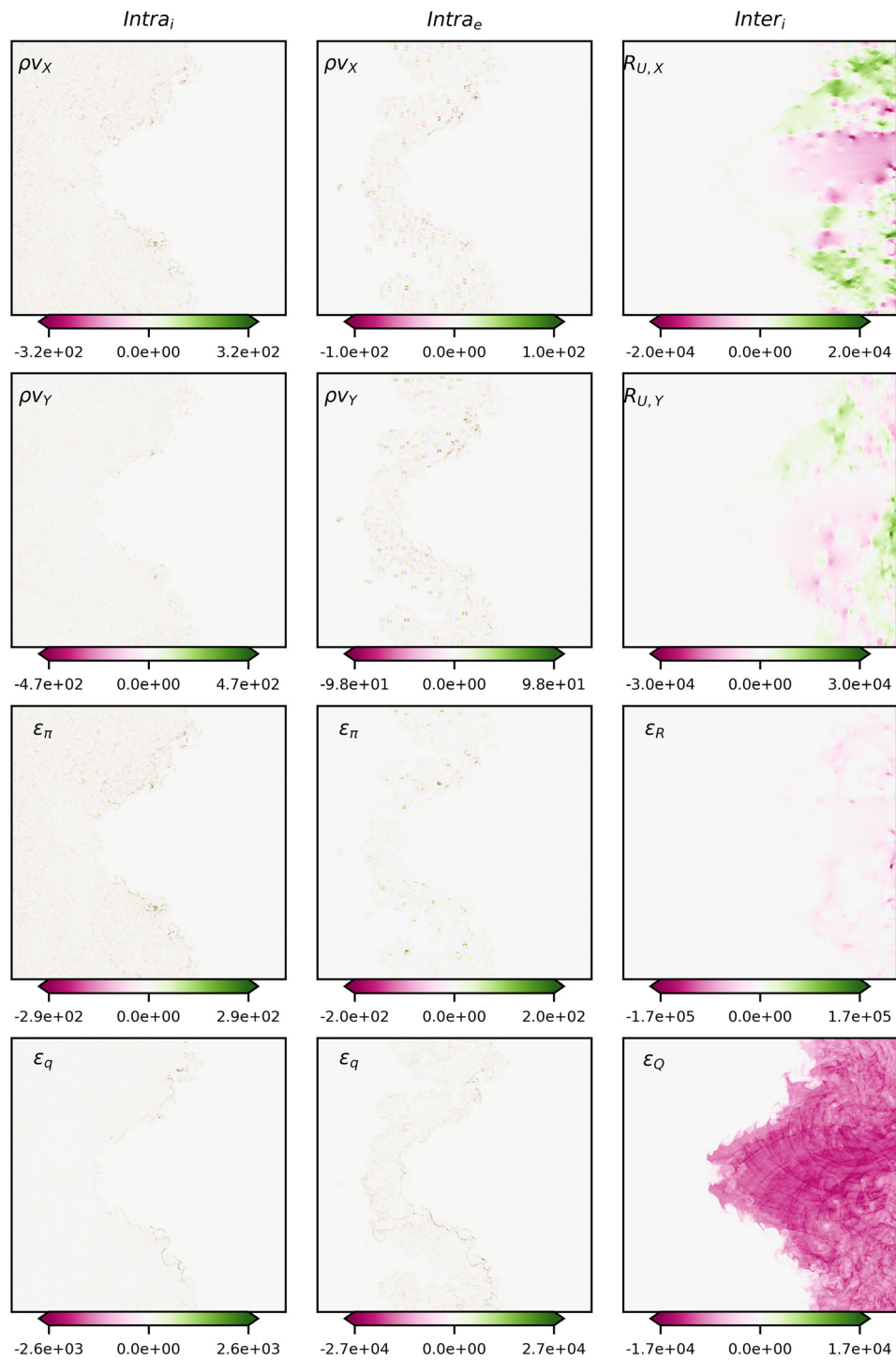
FIG. 11. Contour plots at time $t = 1$ showing the calculated values for the Braginskii transport effects on the conservation equations when applied to the ideal MFP RMI results (after simulation). The simulation result did not include the effect of the Braginskii terms when it was simulated. The columns indicate that intra- or inter-species collisional effects are calculated for the ion or electrons. Each row indicates which Braginskii term is contributing. The variables ρv_x, ρv_y, and ε_π denote the viscous stress contribution to x-momentum-density, y-momentum-density, and energy-density, respectively. ε_q indicates the thermal conductivity effect on energy-density. $R_{U,x}$, $R_{U,y}$, and ε_R denote the influence of inter-species drag on the x-momentum-density, y-momentum-density, and energy-density, respectively. ε_Q indicates the contribution of thermal equilibration to the energy-density.
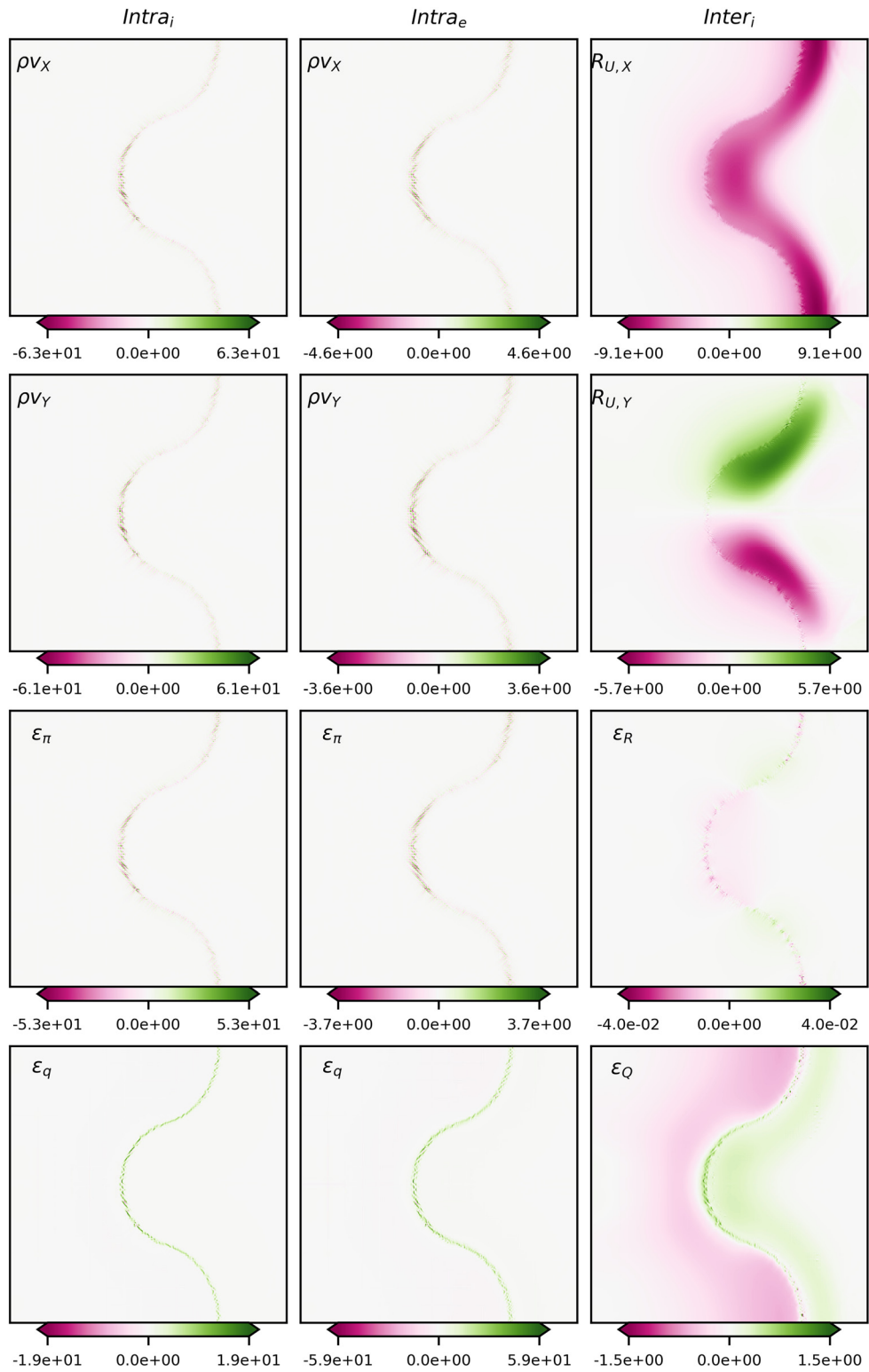
FIG. 12. The effect of the Braginskii transport coefficients on the conservation equations for the full-Braginskii case with anisotropic transport coefficients. Refer to the caption of Fig. 11 which describes the has the same variables and sub-figure ordering.

and strain-rates to develop to magnitudes that would be opposed before forming in the case with transport terms applied.

The inter- and intra-species elastic collisions effect the generation of Z-magnetic fields vary differently. The key factor, which we will continue to encounter repeatedly, is the relative motion between the two species that is permitted by the different retarding forces. The intra-species collisions permit the self-generation of stronger Z-magnetic fields, relative to the inter-species case, through the appreciable current

densities that evolve. The intra-species collisional terms affect each species through the effects of viscosity and thermal conductivity. The transport coefficients within ion and electron fluids for these effects are calculated individually, according to the derivation of Braginskii.[42] The fluid evolutions diverge significantly due to these differing transport coefficients within each species (in addition to differing particle mass and charge), producing strong current densities, greater than even the ideal case at some times, see Fig. 13. The inter-species effects, however,
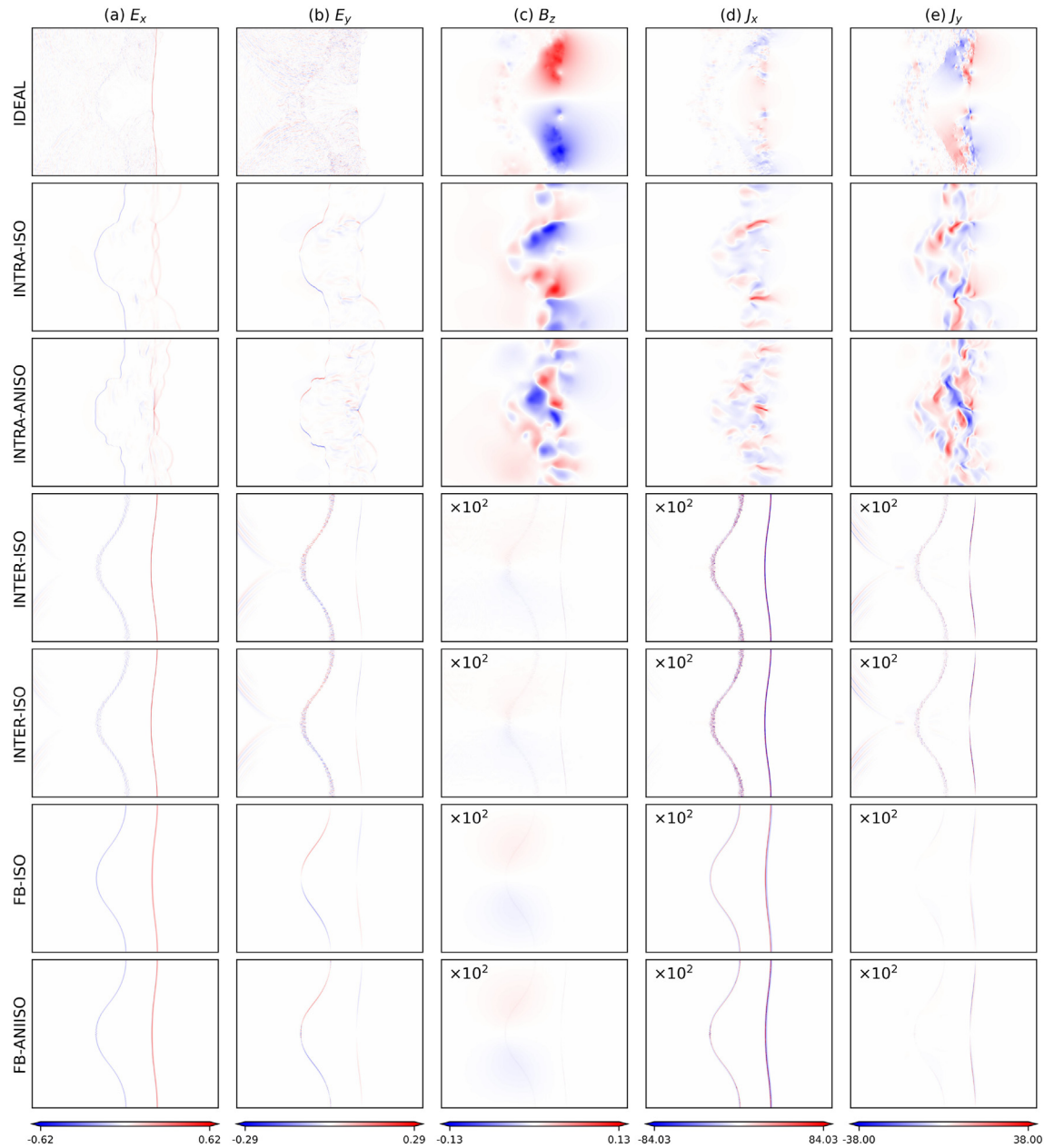

FIG. 13. Contour plots of electromagnetic properties at time $t = 0.5$ non-dimensional time. The properties are (a) x-electric field, (b) y-electric field, (c) z-magnetic field, (d) x-current density, and (e) y-current density.

work to diminish the relative motion, consequently producing current densities that are insignificant in comparison to the intra-species and ideal MFP RMI. The differing evolution of the EM fields is exemplified by Fig. 13 where we see not only the difference in magnitudes but also the sign and regions of action. The ideal and intra-species cases having less terms retarding relative motion produce greater magnitude magnetic fields and more complex EM field arrangements via permitted bulk fluid movements. The inter-species and full-Braginskii cases produce much smaller magnetic fields and homogeneous field orientations in comparison.

Modeling the transport coefficients magnetic field induced anisotropy is important in the case of significant applied or self-generated magnetic field. In the case of the intra-species collisions, the anisotropy in the transport coefficients produces significant differences in the evolution of the RMI. Comparing Figs. 6 and 8, we can see a significant difference in the final time density interface for the two cases. However, we see the inter-species case does not show a significant difference due to the anisotropy because of the insignificant magnetic field generation. In the full-Braginskii case, however, the anisotropy enables the formations of the dual-layer instability, discussed in Sec. VII.

VII. INTERFACE ANALYSIS OF THE MFP RMI WITH FULL-BRAGINSKII TRANSPORT

The evolution of the plasma RMI is dictated by the initial deposition (primary circulation) of baroclinically generated circulation by the initiating shock-wave and the subsequent (secondary circulation) deposition of circulation from electromagnetic fields, the ERTI, and the collisional sources. In the ideal plasma RMI, secondary instabilities are governed by seeding of perturbations at early time (post shock-traversal) and their subsequent amplification through secondary sources of circulation. The elastic collisions fundamentally alter this process—the small perturbations seeded in the ideal, intra-, and inter-species cases are prohibited from forming, and the relative motion of ion and electron fluids (crucial in self-generating electromagnetic fields) is restricted. We may consider the elastic collisions as further reinforcing the coupling between ion and electron fluids that already exists as a result of the Lorentz terms. Additionally, the initial disturbance caused by elastic-collisions in the ion and electron fluids forms a charge density dual-layer that goes unstable. Overall, the plasma RMI with elastic collisions is significantly stabilized and resembles the hydrodynamic solution in terms of growth and large scale features.

The full Braginskii transport terms inhibit the seeding of perturbations on the density interface within both the electron and ion fluids.

The inter-species terms prevent the significant relative motion that generates alternating (in sign) electromagnetic fields that can seed low-wave number perturbations along the density interface. Similarly, the intra-species terms dissipate the high-wave number perturbations that were observed in the inter-species case along the spike and bubble, Fig. 9. The combination of the intra- and inter-species elastic collisions produces a final time density interface that lacks the particular secondary instabilities observed in the intra-species and inter-species cases; however, the dual-layer instability emerges due to these two collisional influences combining.

The necessary conditions for emergence of the dual-layer instability are established prior to the initiating shock arrival at the density interface. The initial temperature discontinuity in the electrons, see Table I, leads to an early time charge density that is intensified by the driving shock traversing the density interfaces: on the interface between zones 1 and 2, thermal conduction is active from the first time step, heating (cooling) the electrons in zone 2 (1), thereby decreasing (increasing) the number density of electrons in zone 2 (1) adjacent to interface. This results is a negative to positive dual-layer in charge density on the interface of zones 1 and 2. Additionally, thermal equilibration between the ions and electrons in zone 2 cools (heats) the ions (electrons), reinforcing the positive charge density in zone 2, and the dual-layer. The resulting electric field accelerates the fluids in opposing directions, a band of electrons in the negative x-direction and a band of ions in the positive x-direction. At the time of RMI-driver shock-wave interaction with its respective density interface, within the ion and electron fluids, the ion interface is ahead of the electron interface—the charge-density distribution is unable to neutralize itself (or oscillate as in the ideal case Bond et al.[18]) prior to the shock-wave arrival because of the inter-species drag term. The shock-waves intensify the dual-layer, but the instability only proceeds in the case where magnetic field induced anisotropy is modeled, see Fig. 14. The anisotropy allows current densities to evolve inhomogeneously along the interface, initiating the dual-layer instability.

The instability begins to develop on the dual-layer through small-scale perturbations attempting to neutralize the charge density, Fig. 15. High-wave number features grow along the extent of the interface but first grow at the spike and bubble; we shall refer to these as dual-layer features (DLF). The absence of the dual-layer instability in the isotropic full Braginskii case points to the anisotropy as the enabling ingredient for the instability. The dual-layer charge density induces electromagnetic fields that work to neutralize the instability. The anisotropic collisional effects provide paths of least resistance for
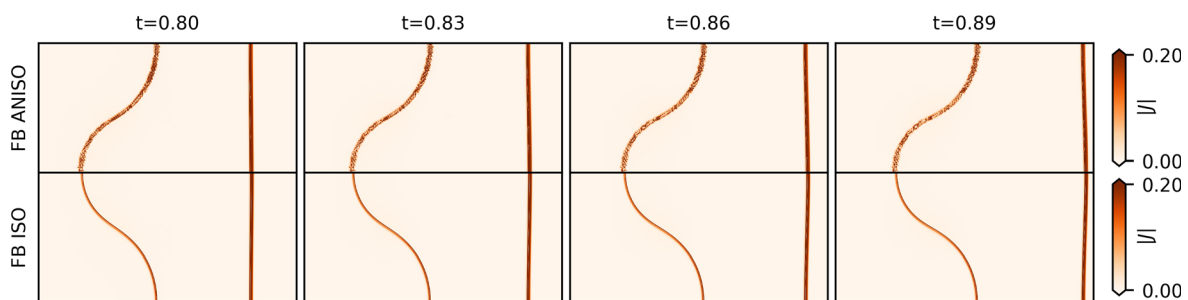

FIG. 14. Magnitude of current density showing the different evolution of the dual-layer in the full-Braginskii anisotropic (top) and isotropic (bottom) cases.
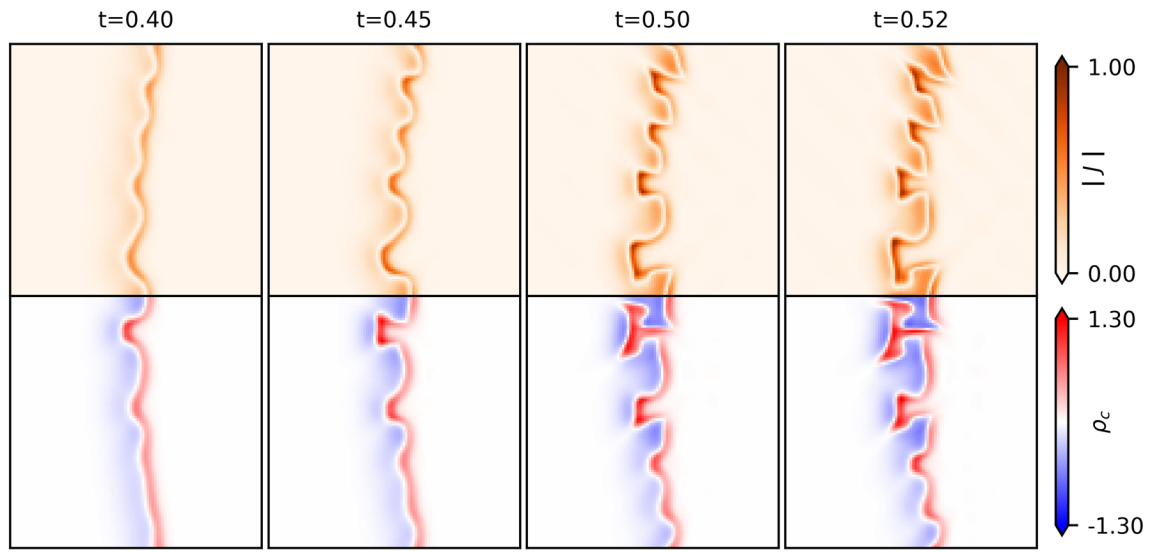
FIG. 15. Magnitude of current density (top) and charge density (bottom) for the full-Braginskii anisotropic case showing the early time evolution on a zoomed view of the spike.

the interface perturbations to evolve into, the momentum contributions applying forces and energy contributions driving changes in the plasma properties, i.e., increasing/decreasing density/pressure. Without anisotropy, the collisional effects provide much more consistent influence (directionally) and do not destabilize the dual-layer. Consider the inter-species drag $\mathbf{R}_u$ (note the following argument holds for thermal force, thermal conductivity, and viscosity) in the isotropic case, the momentum contribution is homogeneous (along the direction of the relative velocity $\mathbf{u} = \mathbf{u}_e - \mathbf{u}_i$); however, in the anisotropic case, there is anisotropy with regard to the component of relative velocity parallel and perpendicular to the magnetic field, and with

regard to the diamagnetic effect (perpendicular to both the magnetic field and relative velocity). This strong anisotropy destabilizes the interface as complex current densities are allowed to evolve (Figs. 16 and 17).

At simulation end, complex DLF proliferate the extent of the primary instability interface. The DLF resemble ERTI mushrooms on the spike/bubble tips, and contorted filaments along the remaining extent of the interface. We see from 17 and 16 that the dual-layer instability, after perturbing the entire extent of the density interface with high-wave number features, produces a charge density distribution that is reduced (in magnitude) along most of the density interfaces. From the
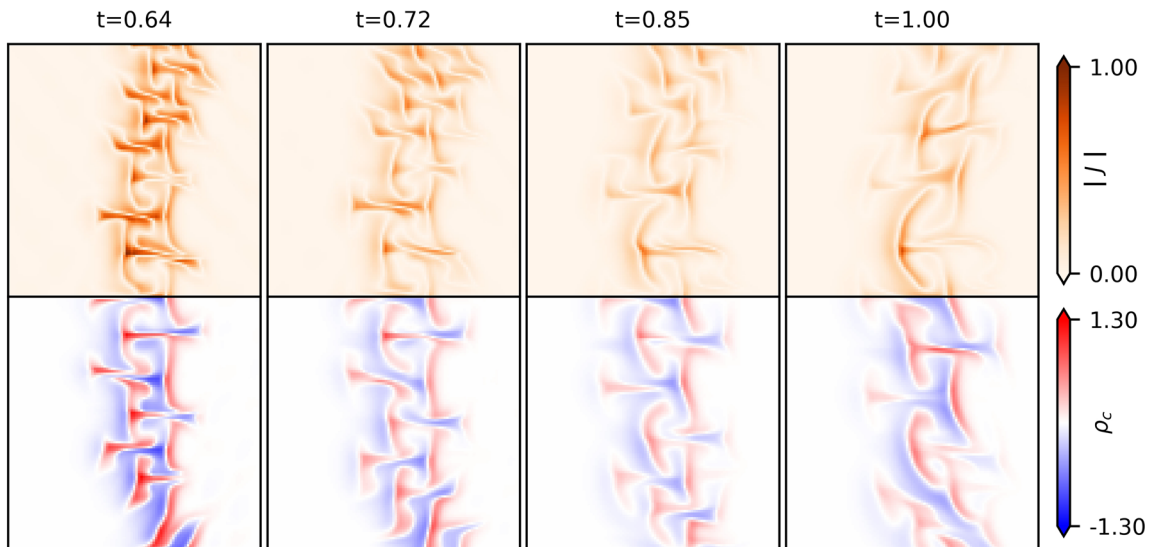

FIG. 16. Magnitude of current density (top) and charge density (bottom) for the full-Braginskii anisotropic case showing for late time a zoomed view of the spike.
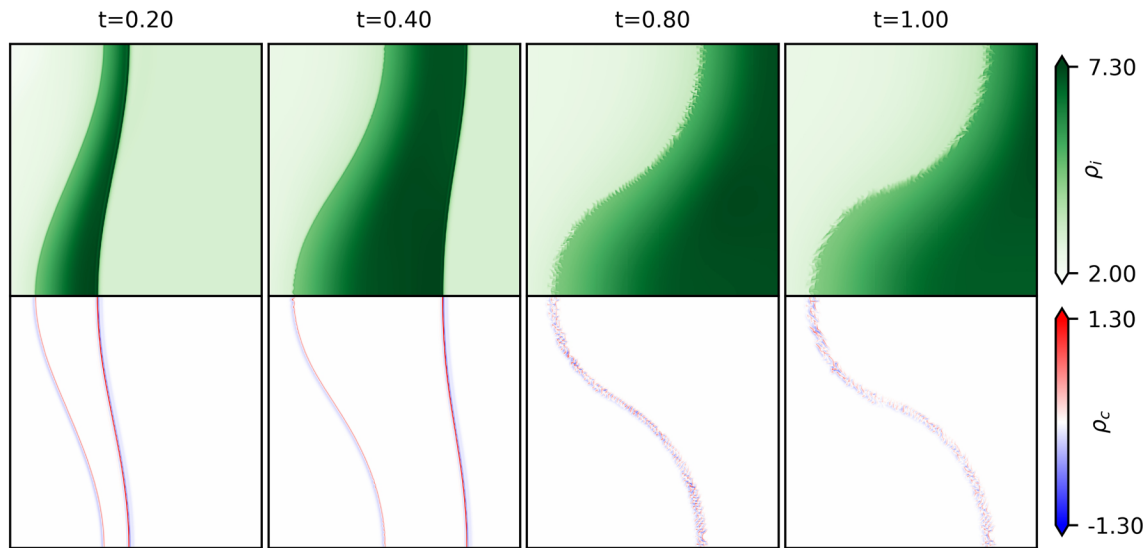
FIG. 17. Ion mass-density (top) and charge density (bottom) for the full-Braginskii anisotropic case showing the full interface development for select times.

onset of the instability to simulation end time, we see the dual-layer becomes highly perturbed, exhibiting localized regions of increased charge density and then a decrease in most regions along the primary instability interface. At simulation end, the dual-layer instability has thickened the density interface along its extent.

The unique deposition of circulation along the density interfaces within the ion and electron fluids produces relative motion between the fluids that influences growth after initial shock traversal. Compare the deposition of circulation for the ion and electron fluids in Fig. 18. Note that in referring to the instabilities, unstable circulation deposition (positive circulation on the lower x-symmetry plane) is considered that which would reinforce the growth of interface amplitude resulting from the primary RMI. All ion fluid sources of circulation, except the viscous term, destabilize the ion fluid density interface during the initial shock traversal ($t \sim 0.05$ to 0.2 non-dimensional time). During the same time within the electron fluid, the baroclinic circulation reinforces the instability, but the inter-species drag driven circulation term stabilizes the instability. The inter-species drag term has a much smaller influence in the ion fluid due to their much greater mass, relative to the electrons. Figure 18 indicates that the electron fluid imparts significant circulation on the ion interface via the inter-species collisions. The DLI begins to affect the interface significantly around $t \sim 0.5$ (Fig. 15 which coincides with common disturbance in the ion and electron rate of circulation deposition). The baroclinic, intra-species, and inter-species terms appear to be the most active during the DLI. The electron and ion fluids experience large negative intra-species (viscous) circulation generation, as the viscous stresses resist the strain that results from the evolution of the DLI perturbations. At this point, the reliability of the interface statistics is questionable as the heuristic used is intended for the primary RMI perturbation and not a DLF proliferated interface that is emerging. An indication of the decreased reliability is the total interface circulation, which becomes non-zero, meaning the interface has lost its symmetry (the half-plane analysis becomes less reliable). Regardless, the interface statistics demonstrate that the DLI affects the interface circulation dynamics in a

localized sense, but may not affect the macro scale evolution, i.e., primary RMI perturbation width, η, as this metric's trend does not change significantly during late time.

The coherence of the electron density interface during the simulation—the electrons do not breakup into a well-mixed region as in loosely coupled cases (Fig. 19)[18,19]—is vital for stabilizing the primary and secondary ion instabilities. A naive cause is that a coherent electron interface reduces the seeding of perturbations along the ion density interface at early times. However, the more significant but nuanced cause is that it allows the fluids to more easily neutralize the charge discontinuity coincident on the ion-fluid density interface that can drive the secondary ERTI and perturb the interface at late time. First, the coherent electron interface produces a charge distribution and associated fields that are localized to the ion density interface. This produces consistent and well behaved fields along the extent of the density interfaces, i.e., there are no significant alternating patterns of EM fields that further develop perturbations and complicated circulation deposition that can seed secondary instabilities. Additionally, the electron density interface matches closely the contour of the ion-interface, allowing the plasma to more easily neutralize the charge density and consequent fields that contribute to the ERTI. Second, the coherent electron density interface can accumulate circulation that then influences the ion interface. The individual circulation depositions the interfaces experience in each fluid produce relative motion between the interfaces which may introduce interesting behavior though further investigation is required. As the dual-layer instability develops, it influences the circulation significantly, seen in Fig. 18 around t 0.5 to 0.75. The complicated structures that emerge from the DLI require a more detailed vorticity analysis heuristic, as the currently used heuristic is only appropriate for the primary RMI perturbation.

VIII. CONCLUSION

Elastic collisions, at the conditions simulated and modeled by the Braginskii transport coefficients, significantly stabilize the MFP RMI. Deposition of circulation dictates the evolution of the RMI and has
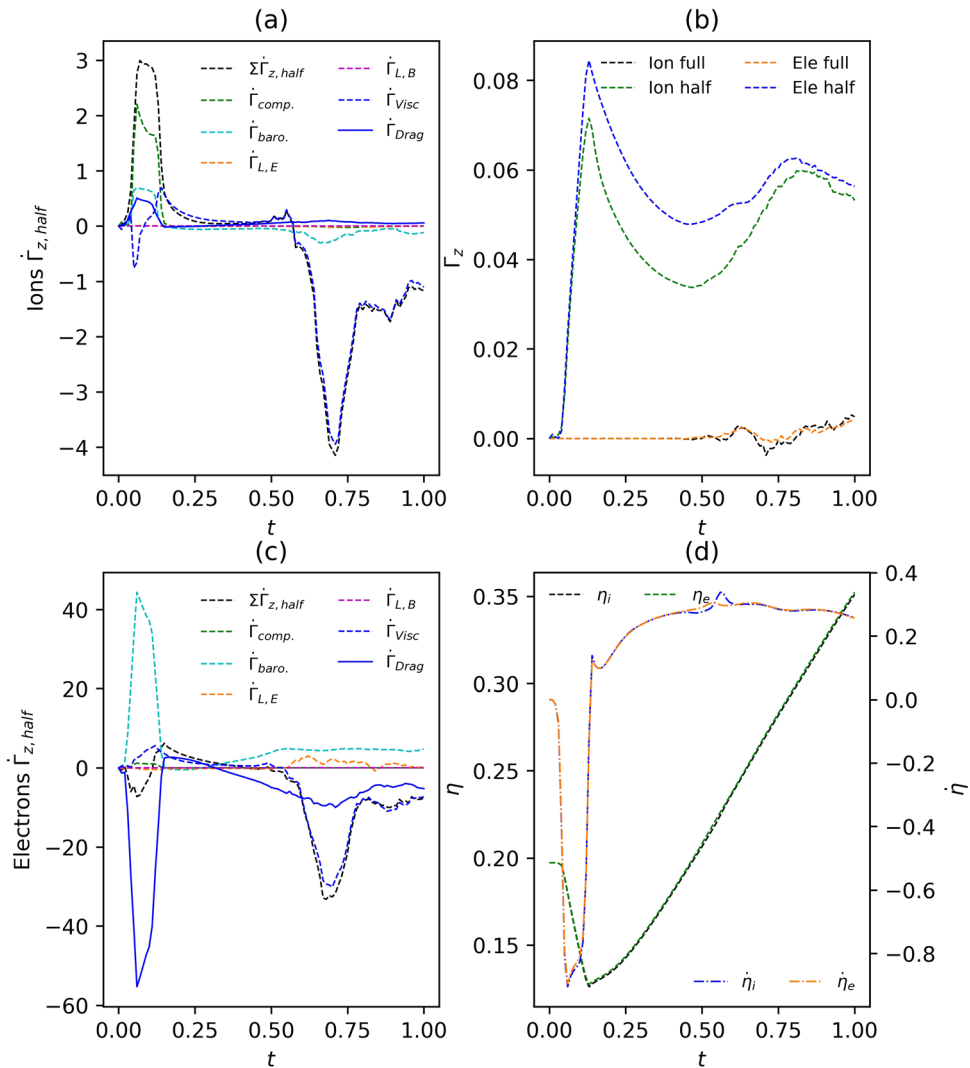
FIG. 18. Deposition of circulation on the ion and electron fluid density interfaces for the MFP RMI with anisotropic full-Braginskii collisions modeled. The most active time is during the shock traversal, where the baroclinic deposition from the shock is evident, as well as the collisional effects. After $t = 0.5$, we observe circulation evolution that corresponds with the dual-layer instability, which does not appear to affect the RMI growth.
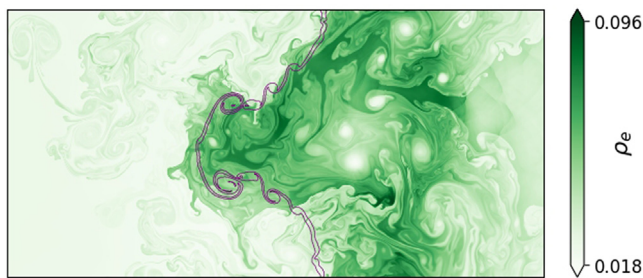

FIG. 19. An example of an electron fluid density interface that has become incoherent and well mixed. The outline of the ion density interface is traced in purple.

many sources in the MFP case. The primary source of circulation is baroclinically generated by the initiating shock traversing the density interface. Secondary circulation is from secondary instabilities, i.e., the ERTI and dual-layer instability, and direct influences, i.e., the electromagnetic torques and elastic collisions. In the ideal plasma RMI, secondary instabilities are governed by seeding of perturbations at early time (post-shock-traversal) and their subsequent amplification through secondary sources of circulation. The full-Braginskii implementation (both intra- and inter-species) of elastic collisions fundamentally alters this process—inter-species collisional terms prohibit the mechanisms observed in the ideal and intra-species cases due to the relative motion between species, and vice versa for the intra-species collisional terms affecting the inter-species mechanisms.

Additionally, the dual-layer that forms in the anisotropic full-Braginskii case, caused by elastic collisions, becomes unstable (though the characteristic scale of the instability is small). The viscous effects within each fluid contribute significant circulation to the density interface during the DLI. The circulation does not appear to affect the primary RMI perturbation, but instead affects the features emerging from the DLI locally—the viscosity resists the deformation and growth of the small scale DLFs. Modeling the magnetic field anisotropy can be important when there is significant externally applied or self-generated magnetic fields—the anisotropic effects alter transport coefficients, leading to varying of RMI evolutions and self-generation of EM fields. Overall, elastic collisions suppress the (1) ERTI of the primary mode perturbation and (2) high-wave number interface perturbation growth mechanisms that were present in the ideal case. The MFP RMI is significantly stabilized and resembles the hydrodynamic solution, a positive result for fusion.

Extension of the current work (two-dimensional three-vector simulations) to full three-dimensional simulations will reveal additional effects with the same underlying principles. The electromagnetic field evolution is a fundamentally three-dimensional phenomena, in that the each field component rate of change is dependent on spatial derivatives in the other dimensions [see the cross product terms in Eqs. 3(a) and 3(b)]. Simulating a 3D perturbation will drive fluid flows and gradients in all spatial dimensions that will generate significant electromagnetic fields in configurations not observed in 2D. These fields will drive evolution of the secondary ERTI in previously unobserved directions, as well as direct Lorentz forcing and EM torques. However, the elastic collisions will still have the same fundamental effects in 3D simulations as for 2D, i.e., the reduction in relative motion between ions and electrons, and dissipation of high-wave number seeded perturbations will still occur. Diamagnetic effects may become more pronounced as significant magnetic field generation permitted in x- and y-directions will produce out of plane forcing. Therefore, we expect the stabilization by the elastic collisions would remain effective in the 3D case with the addition of secondary instabilities in the z-dimension.

ACKNOWLEDGMENTS

AUTHOR DECLARATIONS
Conflict of Interest

The authors have no conflicts to disclose.

Author Contributions

Kyriakos Christos Tapinou: Conceptualization (equal); Data curation (lead); Formal analysis (lead); Investigation (lead); Methodology (equal); Project administration (lead); Validation (lead); Visualization (lead); Writing – original draft (lead); Writing – review & editing (lead). **Vincent Wheatley:** Conceptualization (equal); Data curation (supporting); Investigation (supporting); Supervision (lead); Writing – review & editing (equal). **Daryl Bond:** Conceptualization (equal); Methodology (equal); Supervision (supporting); Validation (equal). **Ingo Jahn:** Supervision (supporting).

DATA AVAILABILITY

The data that support the findings of this study are available from the corresponding author upon reasonable request.

REFERENCES

[1]A. Zylstra, O. Hurricane, D. Callahan, A. Kritcher, J. Ralph, H. Robey, J. Ross, C. Young, K. Baker, D. Casey *et al.*, "Burning plasma achieved in inertial fusion," Nature **601**, 542–548 (2022).

[2]J. Lindl, O. Landen, J. Edwards, E. Moses, and NIC Team, "Review of the national ignition campaign 2009–2012," Phys. Plasmas **21**, 020501 (2014).

[3]S. R. Nagel, K. S. Raman, C. M. Huntington, S. A. MacLaren, P. Wang, M. A. Barrios, T. Baumann, J. Bender, L. Benedetti, D. Doane *et al.*, "A platform for studying the Rayleigh–Taylor and Richtmyer–Meshkov instabilities in a planar geometry at high energy density at the national ignition facility," Phys. Plasmas **24**, 072704 (2017).

[4]B. A. Remington, H.-S. Park, D. T. Casey, R. M. Cavallo, D. S. Clark, C. M. Huntington, C. C. Kuranz, A. R. Miles, S. R. Nagel, K. S. Raman *et al.*, "Rayleigh–Taylor instabilities in high-energy density settings on the national ignition facility," Proc. Natl. Acad. Sci. **116**, 18233–18238 (2019).

[5]C. Zhou and R. Betti, "A measurable Lawson criterion and hydro-equivalent curves for inertial confinement fusion," Phys. Plasmas **15**, 102707 (2008).

[6]J. D. Lawson, "Some criteria for a power producing thermonuclear reactor," Proc. Phys. Soc. Sect. B **70**, 6 (1957).

[7]R. Betti, A. Christopherson, B. Spears, R. Nora, A. Bose, J. Howard, K. Woo, M. Edwards, and J. Sanz, "Alpha heating and burning plasmas in inertial confinement fusion," Phys. Rev. Lett. **114**, 255003 (2015).

[8]C. Walsh, A. Crilly, and J. Chittenden, "Magnetized directly-driven ICF capsules: Increased instability growth from non-uniform laser drive," Nucl. Fusion **60**, 106006 (2020).

[9]P. Radha, V. Goncharov, T. Collins, J. Delettrez, Y. Elbaz, V. Y. Glebov, R. Keck, D. Keller, J. Knauer, J. Marozas *et al.*, "Two-dimensional simulations of plastic-shell, direct-drive implosions on OMEGA," Phys. Plasmas **12**, 032702 (2005).

[10]V. Wheatley, D. Pullin, and R. Samtaney, "Regular shock refraction at an oblique planar density interface in magnetohydrodynamics," J. Fluid Mech. **522**, 179–214 (2005).

[11]V. Wheatley, R. Samtaney, and D. Pullin, "The magnetohydrodynamic Richtmyer-Meshkov instability: The transverse field case," in *Proceedings of the 18th Australasian Fluid Mechanics Conference, Launceston, Australia* (Australasian Fluid Mechanics Society, 2012), pp. 3–7.

[12]V. Wheatley, R. Gehre, R. Samtaney, and D. Pullin, "The magnetohydrodynamic Richtmyer-Meshkov instability: The oblique field case," in *International Symposium on Shock Waves* (Springer, 2013), pp. 1107–1112.

[13]W. Mostert, V. Wheatley, R. Samtaney, and D. Pullin, "Effects of magnetic fields on magnetohydrodynamic cylindrical and spherical Richtmyer-Meshkov instability," Phys. Fluids **27**, 104102 (2015).

[14]W. Mostert, D. Pullin, V. Wheatley, and R. Samtaney, "Magnetohydrodynamic implosion symmetry and suppression of Richtmyer-Meshkov instability in an octahedrally symmetric field," Phys. Rev. Fluids **2**, 013701 (2017).

[15]N. Shen, D. Pullin, V. Wheatley, and R. Samtaney, "Impulse-driven Richtmyer-Meshkov instability in Hall-magnetohydrodynamics," Phys. Rev. Fluids **4**, 103902 (2019).

[16]B. Srinivasan and X.-Z. Tang, "Mechanism for magnetic field generation and growth in Rayleigh-Taylor unstable inertial confinement fusion plasmas," Phys. Plasmas **19**, 082703 (2012).

[17]B. Srinivasan, "Numerical methods for 3-dimensional magnetic confinement configurations using two-fluid plasma equations," Ph.D. thesis (Umi, 2010).

[18]D. Bond, V. Wheatley, R. Samtaney, and D. Pullin, "Richtmyer–Meshkov instability of a thermal interface in a two-fluid plasma," J. Fluid Mech. **833**, 332–363 (2017).

[19]K. Tapinou, V. Wheatley, D. Bond, and I. Jahn, "The Richtmyer-Meshkov instability of thermal, isotope, and species interfaces in a five-moment multi-fluid plasma," J. Fluid Mech. **951**, A11 (2022).

[20]G. Markstein, "A shock-tube study of flame front-pressure wave interaction," Symp. (Int.) Combust. **6**, 387–398 (1957).

[21]R. D. Richtmyer, "Taylor instability in shock acceleration of compressible fluids," Commun. Pure Appl. Math. **13**, 297–319 (1960).

[22]E. Meshkov, "Instability of the interface of two gases accelerated by a shock wave," Fluid Dyn. **4**, 101–104 (1969).

[23]D. Bond, V. Wheatley, R. Samtaney, and D. Pullin, "Electron shock dynamics in the two-fluid plasma Richtmyer-Meshkov instability," in *International Symposium on Shock Waves* (Springer, 2017), pp. 669–676.

[24]M. Hohenberger, P.-Y. Chang, G. Fiksel, J. Knauer, R. Betti, F. Marshall, D. Meyerhofer, F. Séguin, and R. Petrasso, "Inertial confinement fusion implosions with imposed magnetic field compression using the OMEGA laser," Phys. Plasmas **19**, 056306 (2012).

[25]J. D. Bender, O. Schilling, K. S. Raman, R. A. Managan, B. J. Olson, S. R. Copeland, C. L. Ellison, D. J. Erskine, C. M. Huntington, B. E. Morgan *et al.*, "Simulation and flow physics of a shocked and reshocked high-energy-density mixing layer," J. Fluid Mech. **915**, A84 (2021).

[26]Q. Yang, J. Chang, and W. Bao, "Richtmyer-Meshkov instability induced mixing enhancement in the scramjet combustor with a central strut," Adv. Mech. Eng. **6**, 614189 (2014).

[27]J. Yang, T. Kubota, and E. E. Zukoski, "Applications of shock-induced mixing to supersonic combustion," AIAA J. **31**, 854–862 (1993).

[28]W. D. Arnett, J. N. Bahcall, R. P. Kirshner, and S. E. Woosley, "Supernova 1987A," Annu. Rev. Astron. Astrophys. **27**, 629–700 (1989).

[29]D. Arnett, "The role of mixing in astrophysics," Astrophys. J. Suppl. Ser. **127**, 213 (2000).

[30]B. A. Davy and D. T. Blackstock, "Measurements of the refraction and diffraction of a short *N* wave by a gas-filled soap bubble," J. Acoust. Soc. Am. **49**, 732–737 (1971).

[31]R. Stalker and K. Crane, "Driver gas contamination in a high-enthalpy reflected shock tunnel," AIAA J. **16**, 277–279 (1978).

[32]M. Brouillette and R. Bonazza, "Experiments on the Richtmyer–Meshkov instability: Wall effects and wave phenomena," Phys. Fluids **11**, 1127–1142 (1999).

[33]A. M. Khokhlov, E. S. Oran, A. Y. Chtchelkanova, and J. C. Wheeler, "Interaction of a shock with a sinusoidally perturbed flame," Combust. Flame **117**, 99–116 (1999).

[34]A. Khokhlov, E. Oran, and G. Thomas, "Numerical simulation of deflagration-to-detonation transition: The role of shock–flame interactions in turbulent flames," Combust. Flame **117**, 323–339 (1999).

[35]S. Lugomer, "Micro-fluid dynamics via laser–matter interaction: Vortex filament structures, helical instability, reconnection, merging, and undulation," Phys. Lett. A **361**, 87–97 (2007).

[36]W. Buttler, D. Oró, D. Preston, K. O. Mikaelian, F. Cherne, R. Hixson, F. Mariam, C. Morris, J. Stone, G. Terrones *et al.*, "Unstable Richtmyer–Meshkov growth of solid and liquid metals in vacuum," J. Fluid Mech. **703**, 60–84 (2012).

[37]M. Brouillette, "The Richtmyer-Meshkov instability," Annu. Rev. Fluid Mech. **34**, 445–468 (2002).

[38]Y. Zhou, "Rayleigh–Taylor and Richtmyer–Meshkov instability induced flow, turbulence, and mixing. II," Phys. Rep. **723**, 1–160 (2017).

[39]Y. Zhou, R. J. Williams, P. Ramaprabhu, M. Groom, B. Thornber, A. Hillier, W. Mostert, B. Rollin, S. Balachandar, P. D. Powell *et al.*, "Rayleigh–Taylor and Richtmyer–Meshkov instabilities: A journey through scales," Physica D **423**, 132838 (2021).

[40]M. Rosenberg, H. Rinderknecht, N. Hoffman, P. Amendt, S. Atzeni, A. Zylstra, C. Li, F. Séguin, H. Sio, M. G. Johnson *et al.*, "Exploration of the transition from the hydrodynamiclike to the strongly kinetic regime in shock-driven implosions," Phys. Rev. Lett. **112**, 185001 (2014).

[41]H. G. Rinderknecht, M. Rosenberg, C. Li, N. Hoffman, G. Kagan, A. Zylstra, H. Sio, J. Frenje, M. G. Johnson, F. Séguin *et al.*, "Ion thermal decoupling and species separation in shock-driven implosions," Phys. Rev. Lett. **114**, 025001 (2015).

[42]S. Braginskii, "Transport processes in a plasma," Rev. Plasma Phys. **1**, 205–311 (1965).

[43]T. Berlok, R. Pakmor, and C. Pfrommer, "Braginskii viscosity on an unstructured, moving mesh accelerated with super-time-stepping," Mon. Not. R. Astron. Soc. **491**, 2919–2938 (2020).

[44]J. D. Sadler, C. A. Walsh, and H. Li, "Symmetric set of transport coefficients for collisional magnetized plasma," Phys. Rev. Lett. **126**, 075001 (2021).

[45]Z. Li and D. Livescu, "High-order two-fluid plasma solver for direct numerical simulations of plasma flows with full transport phenomena," Phys. Plasmas **26**, 012109 (2019).

[46]U. Shumlak, R. Lilly, N. Reddell, E. Sousa, and B. Srinivasan, "Advanced physics calculations using a multi-fluid plasma model," Comput. Phys. Commun. **182**, 1767–1770 (2011).

[47]E. Meier and U. Shumlak, "Development of five-moment two-fluid modeling for z-pinch physics," Phys. Plasmas **28**, 092512 (2021).

[48]S. Miller, "Modeling collisional processes in plasmas using discontinuous numerical methods," Ph.D. thesis (University of Washington, 2016).

[49]D. Bond, V. Wheatley, Y. Li, R. Samtaney, and D. Pullin, "The magnetised Richtmyer–Meshkov instability in two-fluid plasmas," J. Fluid Mech. **903**, A41 (2020).

[50]J. Loverich, "A finite volume algorithm for the two-fluid plasma system in one dimension," Ph.D. thesis (University of Washington, 2003).

[51]E. Epperlein and M. Haines, "Plasma transport coefficients in a magnetic field by direct numerical solution of the Fokker–Planck equation," Phys. Fluids **29**, 1029–1041 (1986).

[52]J. Davies, H. Wen, J.-Y. Ji, and E. D. Held, "Transport coefficients for magnetic-field evolution in inviscid magnetohydrodynamics," Phys. Plasmas **28**, 012305 (2021).

[53]I. Kotelnikov, "Braginskii and Balescu kinetic coefficients for electrons in Lorentzian plasma," Plasma Phys. Rep. **38**, 608 (2012).

[54]W. Zhang, A. Almgren, V. Beckner, J. Bell, J. Blaschke, C. Chan, M. Day, B. Friesen, K. Gott, D. Graves *et al.*, "AMReX: A framework for block-structured adaptive mesh refinement," J. Open Source Software **4**, 1370–1370 (2019).

[55]S. Gottlieb, C.-W. Shu, and E. Tadmor, "Strong stability-preserving high-order time discretization methods," SIAM Rev. **43**(1), 89–112 (2001).

[56]B. Van Leer, "Towards the ultimate conservative difference scheme. V. A second-order sequel to Godunov's method," J. Comput. Phys. **32**, 101–136 (1979).

[57]E. F. Toro, M. Spruce, and W. Speares, "Restoration of the contact surface in the HLL-Riemann solver," Shock Waves **4**, 25–34 (1994).

[58]J. A. Moreno, E. Oliva, and P. Velarde, "EMcLAW: An unsplit Godunov method for Maxwell's equations including polarization, metals, divergence control and AMR," Comput. Phys. Commun. **260**, 107268 (2021).

[59]R. Abgrall and H. Kumar, "Robust finite volume schemes for two-fluid plasma equations," J. Sci. Comput. **60**, 584–611 (2014).

[60]R. Samtaney, "Suppression of the Richtmyer–Meshkov instability in the presence of a magnetic field," Phys. Fluids **15**, L53–L56 (2003).

[61]P. Keiter, R. Drake, T. Perry, H. Robey, B. Remington, C. Iglesias, R. Wallace, and J. Knauer, "Observation of a hydrodynamically driven, radiative-precursor shock," Phys. Rev. Lett. **89**, 165003 (2002).

[62]G. Yamada, M. Kajino, and K. Ohtani, "Experimental and numerical study on radiating shock tube flows for spacecraft reentry flights," J. Fluid Sci. Technol. **14**, JFST0022 (2019).

[63]S. Hu, V. Goncharov, T. Boehly, R. McCrory, S. Skupsky, L. A. Collins, J. D. Kress, and B. Militzer, "Impact of first-principles properties of deuterium–tritium on inertial confinement fusion target designs," Phys. Plasmas **22**, 056304 (2015).

[64]D. Ghosh, T. D. Chapman, R. L. Berger, A. Dimits, and J. Banks, "A multispecies, multifluid model for laser–induced counterstreaming plasma simulations," Comput. Fluids **186**, 38–57 (2019).

[65]P. Rambo and R. Procassini, "A comparison of kinetic and multifluid simulations of laser-produced colliding plasmas," Phys. Plasmas **2**, 3130–3145 (1995).

[66]O. S. Jones, U. Shumlak, and D. S. Eberhardt, "An implicit scheme for nonideal magnetohydrodynamics," J. Comput. Phys. **130**, 231–242 (1997).